University of Alberta

Exploring the Use of Nuclear Magnetic Resonance to Examine Spinal Cord Injury

By

Daniel Patrick Hallihan

A thesis submitted to the Faculty of Graduate Studies and Research in partial fulfillment of the requirements for the degree of

Master of Science

Department of Biomedical Engineering

Spring 2013
Edmonton Alberta

1. Abstract

Spinal cord injury is most commonly caused by physical trauma, and the resulting functional loss can vary considerably in both degree, extent and location. Understanding what spinal cord tissue is damaged and to what degree can be useful in both determining the appropriate treatment for individuals with spinal cord injury and for assessing novel methods of treatment. This thesis looks at the applications of nuclear magnetic resonance (NMR), to assess spinal cord injury, assess the effects of various treatments and assist in developing new treatments of spinal cord injury. The treatment of interest in this thesis is intra-spinal micro-stimulation (ISMS), a method of functional electrical stimulation (FES). Magnetic resonance imaging (MRI) provided grey/white matter contrast in images and ISMS micro-wire localization, water compartmentalization showed promise in determining myelination, and nuclear magnetic resonance spectroscopy (MRS) found several metabolites that varied due to spinal cord injury and could potentially be measured in-vivo.

Acknowledgements

I would like to thank my supervisors, Dr. Peter S. Allen, and Dr. Vivian Mushawar for their incredible support and patience in helping me see this degree thought to the end.

Contents

List of Figures

List of Symbols and Abbreviations

NMR ---------- Nuclear Magnetic Resonance

CT ---------- Computed Tomography

PET ---------- Positron Emission Tomography

FES ---------- Functional Electronic Stimulation

ISMS ---------- Intra-Spinal Micro-Stimulation

MRI ---------- Magnetic Resonance Imaging

MRS ---------- Magnetic Resonance Spectroscopy

GLAST ---------- Glutamate Aspartate Transpoter

GLT-1 ---------- Glutamate Transporter

1

I ---------- Spin Angular Momentum of a Nucleus

μ ---------- Magnetic Moment

γ ---------- Gyromagnetic Ratio

h ---------- Plank's Constant

$\vec{B}_0$ ---------- Static Magnetic Field

E ---------- Energy

m ---------- Quantum Number

$\hbar$ ---------- Reduced Plank's Constant

ΔE ---------- Energy Difference Between Spin States

k ---------- Boltzmann's Constant

$\vec{M}$ ---------- Observable Magnetic Moment

ω ---------- Angular Frequency

$\vec{B}_1$ ---------- Applied Magnetic Field

FID ---------- Free Induction Decay

T_1 ---------- Longitudinal Recovery Constant

T_2 ---------- Transverse Relaxation Constant

$\vec{B}_L$ ---------- Time Dependant Local Dipolar Field

$J(\omega)$ ---------- Debye Spectral Density

τ_c ---------- Correlation Time

T_2' ---------- Incremental Relaxation Constant

T_2^* ---------- Combined Relaxation Constant

G ---------- Magnetic Field Gradients

f ---------- Frequency in Hertz

ppm ---------- Parts Per Million

1. Overview of Thesis

The overall goal of this thesis work was to evaluate nuclear magnetic resonance (NMR) as an appropriate method for examining the chemical and morphological consequences of spinal cord injury in the tissue surrounding the site of the injury. In addition to examining the primary injury, monitoring the progression of secondary injury, and evaluating the effectiveness potential treatments are important clinical tasks for which NMR may be suitable. Currently, clinical examination of the chemical changes in the human spinal cord requires invasive techniques, such as lumbar puncture, that can only be repeated a limited number of times and can have undesirable side effects [1,2]. Moreover, a lumbar puncture only samples the cerebral spinal fluid, thereby providing limited information regarding the health of the cells in the spinal cord. Other imaging techniques, such as X-ray, X-ray computed tomography (CT), positron emission tomography (PET), and ultrasound, of the spinal cord exist, which can provide some limited morphological information; nevertheless, more information should be obtainable using NMR. In this thesis work I evaluated non-invasive methodologies that

can be performed repetitively, and at the same time provide more detailed information than the methods that are currently in use.

Spinal cord injuries, which are described more fully in section 2.1, occur at an annual rate of 32 cases per million population, and there are approximately one third of a million people, already living with spinal cord injury in North America [3,4,5]. It is an injury most commonly caused by motor vehicle accidents; the next most common cause is falls [4]. Spinal cord damage may also be the result of a disease [3]. In addition to the extent of this initial trauma, it is necessary to monitor the progression of secondary injury over time. Information about the initial injury and the progression of secondary injury can then be used to determine what clinical interventions should be implemented. For example, if the injury is incomplete, as most are, rehabilitation methods like training, drugs and externally applied functional electrical stimulation (FES) may be appropriate. If the injury is complete, more aggressive treatments such as stem cells or implanted FES systems including intra-spinal microsimulation (ISMS) may be necessary to restore function. Following these interventions, the outcome

needs to be monitored to determine how successful they are and whether or not further intervention is required to restore function.

As stated before, the purpose of this thesis work was to evaluate various NMR techniques as a method for monitoring spinal cord injury. It is both non-invasive and capable of being used repetitively. One NMR technique, magnetic resonance imaging (MRI), can provide much of the morphological information that is required to asses injury and the effects of treatment. In addition, MRI can also assist in preoperative planning for interventions that require surgery. Going beyond basic imaging it is possible to use NMR to perform water compartment analysis which provides information on the relative distribution of water at the cellular level. Specifically, separating water in myelin from water in other cellular and extracellular compartments and subsequently characterizing the freedom of water in both, can in turn characterize the extent of morphological damage induced by the injury. Exploiting the spectroscopic power of NMR MRS, it becomes possible to identify and quantify many of the important chemical compounds in the spinal cord, together with the changes that might occur to these

compounds after a spinal cord injury. Knowing what chemical changes are occurring and eventually being able to measure them in-vivo can both evaluate the effectiveness of drug treatments and assist in determining the type and dosage of potential treatments. Performing in-vivo MRS is challenging and must typically focus on one or two chemicals at a time. To determine on what chemicals to focus in-vivo, in-vitro MRS studies were conducted on excised tissue using a very high field strength NMR system that enabled numerous chemicals to be examined at once. The chemicals examined in this study were neurotransmitters such as glycine[7], glutamate [8,9,10,11] glutamine [10], GABA [11] cellular markers such as myo-Inositol[10], and others metabolites that changed due to spinal cord injury in previous studies [11,12,13,14,15,16].

MRI was able to provide adequate pre-operative images of the spinal cord, as shown in chapter 4 figure 4.1, 4.2, and 4.3; showing grey matter/ white matter contrast that may be valuable in assessing injury or assisting in surgical treatments. The MRI of ISMS micro-wires, though only conducted on extracted tissue samples, showed that wire position varied considerably from the vertical as can be seen in figure 4.4. This realization initiated

changes in the process of micro-wire implantation to ensure that the wires are inserted vertically. Water compartmentalization was able to detect two of the four compartments known from previous studies, myelin water and other water, and showed variation with distance from injury as seen in figure 4.6. Without histological verifcation it is not possible to confirm the exact meaning of these changes but the higher myelin water fraction might indicate axonal degeneration. High field MRS showed changes in myo-Inositol, and NAAG. Looking specifically at the difference from the control sample and the experimental sample at various time points NAA, glutamine, creatine, and choline all showed changes as shown in figure 4.8-12. Finally using a clinical sized 3T magnet, NAA, creatine, and choline were detectable in-vivo.

2. Background Information

2.1 Spinal Cord Injury

2.1.1 Primary Injury

Primary injury is the initial injury usually caused by direct physical trauma to the spinal column from the sources listed in the overview. This often breaks the vertebrae that protect the spinal cord, and can severely deform the cord which in turn disrupts the blood vessels, neurons, and glial cells that make up the spinal cord itself. In some models of spinal cord injury such as the “weight drop” model, the grey matter at the center of the spinal cord is exposed to the greatest mechanical stress and suffers the most damage [17]. The grey matter is the location of the cell bodies of neurons in the spinal cord; the surrounding white matter contains the myelinated axons of these neurons, ascending axons of sensory neurons as well as descending axons of neurons from the brain and brain stem. These axons are of little use without their associated cell bodies and will decay soon after injury. Differentiating the grey and white matter is difficult

using techniques such as X-ray, because the two tissues have similar density, or biopsies for histology, as taking even a small tissue sample permanently damages the spinal cord. Fortunately, the water NMR relaxation time between the two tissues (used in MRI as a contrast mechanism), varies enough to make differentiating grey and white matter possible.

Spinal cord injury is classified by both the severity of the injury and its location. Injuries to the cervical spinal cord, the region encased by the 7 cervical vertebrae, cause tetraplegia; injuries below this level cause paraplegia. The injury is considered physiologically complete when there is no sensation or muscle control in regions of the body below the injury. In incomplete injury, some neurons still cross the injured region providing either some motor control or sensation below the lesion site. Incomplete tetraplegia accounts for 31.2%, complete paraplegia 28.2%, incomplete paraplegia 23.1%, and complete tetraplegia for 17.5% [3,4,5] of all spinal cord injuries.

2.1.2 Secondary Injury

After the initial injury, secondary processes involving

vascular, cellular, and biochemical changes take place. These were initially demonstrated by Allen in 1911 [17], who showed that removal of damaged tissue improved the neurological function of the remaining cord. These secondary changes initially take place in the grey matter and then progress into the white matter [18,19]. The secondary injury also progresses rostrally and caudally from the site of primary injury. The following sections briefly discuss the vascular, cellular and biochemical pathways of secondary injury.

2.1.2.1 Vascular Changes

Immediately after injury, which is typically a compression injury, there is a decreased rate of blood flow to the damaged area, leaving the tissue of the spinal cord under perfused. Injury generally causes differential changes in grey/white matter perfusion. In some studies, perfusion of the white matter dropped from 1 hour to 8 hours after injury and recovered by 24 hours after injury [18]. In other studies, white matter perfusion was below normal for 1 hour post-injury but significantly increased by 24 hours post-injury [18], and grey matter perfusion remained low for 24 hours [18]. Along with the decreased blood

flow, there is also superficial haemorrhaging that progresses both rostrally and caudally from the site of initial injury [22]. The haemorrhaging is more severe in the grey matter [23] as vessels in the grey matter are more susceptible to injury than white matter vessels [18]. Haemorrhaging continues to increase from one to 4 hours after the initial injury [18]; this haemorrhaging eventually leads to necrosis of the grey matter.

In addition to the loss of blood flow, the spinal cord also loses its micro environment. Like a brain, the spinal cord has a barrier that separates it from the circulatory system allowing the spinal cord to filter out potentially damaging substances and cells. The blood spinal cord barrier breaks down in spinal cord injury allowing these cells and proteins not normally present in the central nervous system into the spinal cord. The breakdown is partly due to the loss of anionic charge on the the endothelial cells forming the luminal surface of the barrier, which normally keeps negatively charged proteins out [24]. This breakdown of the blood spinal cord barrier extends along the axis of the injured cord reaching its maximal extent 1 day after injury and then declining [22]. The disruption of the blood spinal cord barrier lasts from 4 to 28 days; this disruption of the barrier allows

inflammatory cells into the spinal cord, and can permit the entrance of amino acids in toxic levels [24] as well.

2.1.2.2 Cellular Changes

Within hours after the initial injury, macrophages from the blood stream and activated microglia from surrounding tissue migrate to the site of the injury. The activated microglia divide and become more like macrophages with time. Both cells remain in the injury site clearing debris for weeks after the injury [25]. Meningeal cells also rapidly migrate to the site of injury to repair any meninges that have been damaged by the primary injury [25]. They also reform the glia limitans with astrocytes that migrate to the injury. Oligodendrocyte precursor cells also migrate to the site of a demyelinated injury peaking 7 days after the initial injury and then declining over a period of several weeks [25]. Astrocytes are the predominant cell found in the glial scar that forms after an injury. Astrocytes become hyper trophic, producing many fine processes as well as dividing to form a glial scar of tightly packed hyper filamentous cells with their processes filling most of the extracellular space connected with gap and tight junctions [25]. This glial scar is inhibitory to

axonal regrowth both as a physical barrier and by secreting growth inhibiting compounds.

2.1.2.3 Biochemical Changes

Cells such as neutrophils, macrophages and lymphocytes that infiltrate the spinal cord initiate inflammation after injury. Inflammation is a normal response of the body to injury or foreign substances. Neutrophils (within the first 24 hours) and then lymphocytes (which reach peak concentrations in 48 hours) infiltrate the spinal cord from the circulatory system [18]. Neutrophils secrete myeloperoxidase and lymphocytes increase the concentration of cytokines, chemokines and growth factors in the spinal cord [19]. Inhibitory factors and barriers to regeneration are expressed in the growing site of the lesion, which prevent neuronal regrowth. Slowing the expression of these factors with hypothermia [20] or drugs such as methylprednisolone [21] can improve the number of neurons spared and functional recovery. However, some of the cytockines being produced such as tumor necrosis factor, are needed for neuron regrowth.

Free radicals are reactive molecules that have an unpaired

electron in their outer shell and are therefore highly reactive. Small amounts of free radicals are normally produced in the spinal cord as part of the mitochondrial electron transport chain; they also influence N-methyl-D-aspartate (NMDA) receptor function. After spinal cord injury when the tissue is reperfused, the break down of the blood spinal cord barrier allows transition metals like iron and copper and haemoglobin decay products like haematin to come in direct contact with the spinal cord neurons and glial cells. Iron, copper and other transition metals can very easily gain or lose electrons which causes them to act as catalysts to produce free radicals. The most common free radicals involved in spinal cord injury are oxygen derived such as O_2^-, H_2O_2, and OH^-. These free radicals react with polyunsaturated fatty acids found in cell membranes. Lipid per oxidation, where oxygen derived free radicals react with lipids to form lipid free radical intermediates and fatty acid hydro-peroxides, can be a geometrically progressing chain reaction if catalysts such as iron are present[26]. Nitric oxide (NO) which is also produced in small amounts in the central nervous system and is not by itself harmful, reacts with O_2^- to produce $ONOO^-$, that can oxidize proteins and DNA as well as lipids causing significant neuronal

loss. NO concentration sharply increases after spinal cord injury and then decreases between 1 and 12 days after injury [26,27].

In addition to the damage from factors invading the spinal cord after injury many of the spinal cords internal metabolites also malfunction. Levels of extracellular excitatory amino acids, particularly the major excitatory neurotransmitter glutamate, increase dramatically after injury reaching cytotoxic levels [28]. Glutamate reaches peak concentration in 15 minutes after injury. It returns to normal levels within 1.5 hours after injury [28]. Normally, glutamate is cleared from the synaptic cleft by glutamate transporter proteins glutamate aspartate transporter (GLAST) and glutamate transporter 1 (GLT-1) which are found in the glial cells; these transfer proteins along with other such as EAAC1; transport glutamate against the 1000 fold concentration gradient to clear it from the synapse [29]. These transporter proteins do not peak until 6 hours after injury and remain high for 24 hours after injury [29]. This gives time for excitotoxicity where glutamate and aspartate are at high enough levels to destroy neurons through prolonged excitation. The excess glutamate causes Ca++ to move into the neurons through α-amino-3-hydroxy-5-methyl-4-isoxazole propionate (AMPA)/

kainate receptors and to a lesser degree through NMDA receptors [30]. Intracellular Ca^{++} and Na^{+} accumulate in the mitochondria and this irreversibly damages the mitochondria and causes ATP depletion leading to cell death. Studies have even shown a decrease in glutamate levels from 4 hours to 12 hours after spinal cord injury compared to sham injury [31]. The same study shows that glutamine increases at 4 and 8 hours after spinal cord injury compared to sham injury and that the sum of glutamate and glutamine remained constant. Other metabolites are also influenced by spinal cord injury. Aspartate declines by 4 hours after injury and remains low till at least 12 hours after injury [31]. γ-aminobutyric acid (GABA) the primary inhibitory amino acid increases from 2 hours to 12 hours post-injury compared to sham controls [32]. Glycine, another inhibitory amino acid shows no change in this study [31]. Taurine which is not a neurotransmitter though it does play a role in Ca^{++} regulation after glutamate stimulation, showed increased levels compared to the sham group only at 4 hours post-injury.

2.1.3 Interventions

Spinal cord tissue is part of the central nervous system

which has limited capacity of repair following an injury. Immediately after injury, immobilization with neck collars and spinal boards, is implemented. Drugs, such as Methylprednisolone, hypothermia and surgery to remove damaged tissue and bone fragments, can prevent further injury [33]. After the injury is stabilized, rehabilitation through physiotherapy can be used to utilize remaining functionality for new tasks. Remaining functionality can also be augmented with specialized wheelchairs and other electronic devices to improve quality of life. FES uses electrodes placed on muscles or nerves below the injury to activate these muscles [34]. A more invasive method that might have broader applications is ISMS in which micro-wires are implanted in the spinal cord below the injury, typically in the lumbar enlargement. These wires can then be used to stimulate the neurons in the spinal cord to control bladder and bowel function and limb moments such as walking [35].

2.1.4 Conclusions

It can be seen that after the initial physical damage to the spinal cord important changes occur. In the vascular system

there is reduced perfusion, haemorrhaging that may lead to necrosis, and a breakdown of the blood spinal cord barrier causing loss of the spinal cord's micro environment. Cells such as microglia and macrophages migrate to the site of the injury to clear away debris, meningeal cells attempt to repair the damaged meninges, and cells such as astrocytes form a glial scar preventing neural regrowth. Inflammation which prevents infection, assists in removing debris, and can promote healing but also increases the number of neurons lost because of the injury[36]. Transition metals from the blood stream create free radicals that damage proteins, lipids, and DNA. The tight regulation of metabolites in the spinal cord is also lost and some metabolites such as glutamate reach cytotoxic levels.

Using X-ray or CT it is possible to examine the damage to the spine and deformation of the spinal cord. With contrast agents it is even possible to assess the blood flow to the spinal cord. There are several disadvantages with using CT, such as the need for contrast agents, the poor grey/white matter contrast, the inability to detect any of the biochemical changes in the spinal cord, and the radiation exposure limits the number of scans that can be performed. To monitor the biochemical and

cellular changes in the spinal cord a possible option is to perform a spinal tap. This procedure takes a sample of the cerebral spinal fluid that can then be assessed in vitro; this allows the overall state of the spinal cord to be analyzed but unfortunately does not provide spatial localization. For better localization a spinal cord biopsy could be obtained; however the spinal cord's inability to regenerate makes taking tissue samples highly undesirable. NMR is able to bypass many of these problems; it has good grey/white matter contrast, does not require a contrast agent to assess blood flow, it can monitor biochemical changes in-vivo, albeit with limited spatial resolution, and can characterize the chemical changes due to injury. NMR has no known side effects, though there are a few contraindications such as metallic implants or large tattoos. All of this makes NMR a powerful method to observe spinal cord injury, its progression, and the effect of potential treatments. Since the focus of my work is on using NMR to assess spinal cord injury, the next section will illustrate some of the basic principles of NMR.

2.2 Basics of Nuclear Magnetic Resonance

2.2.1 Magnetism of Nuclei

The microscopic constituents of matter can be considered to have three basic properties: mass, electrical charge, and spin angular momentum, which can, in turn, give rise to spin magnetic moment. Mass and electrical charge determine many of the thermal and chemical properties of matter which are observable on the macroscopic scale. Magnetism, though in general much weaker and therefore harder to observe, can also be detected on a macroscopic scale in a few materials, with transition elements. Spin manifests itself macroscopically, principally though it's interconnection with magnetism. Though, when working at the macroscopic scale it is sometimes tempting or even convenient to think of spin as rotating angular momentum, this would really be a stretch too far, because spin is an intrinsic property of microscopic matter and not a form of kinetic energy.

Electrons, neutrons, and protons all exhibit the property of spin, and for each particle it has a value of one half. The combination of the individual spins of the neutrons and protons

in a nucleus determines the overall spin of that atomic nucleus, and is usually given the symbol, (I). Not all nuclei have an observable spin and therefore resultant magnetic moment. To do so the nucleus must have an odd number of protons and or neutrons. Nuclei such as, $^{1}_{1}H$ $^{13}_{6}C$, $^{31}_{15}P$ all have a spin of one half. $^{1}_{1}H$ is perhaps one of the most biologically significant of these because $^{1}_{1}H$ is the overwhelmingly dominant naturally occurring isotope of hydrogen, and because hydrogen is ubiquitous in the body both, in water and in most other biological molecules. Unlike $^{1}_{1}H$, $^{13}_{6}C$ is not the dominant isotope of carbon i.e. only 1.1% of carbon is $^{13}_{6}C$.

The magnetic moment (μ) of a nucleus is related to the nuclear spin angular momentum I, by

$$\mu = \frac{\gamma h I}{2\pi} \qquad [2.1]$$

where the proportionality constant, γ, is called the gyromagnetic ratio of the nucleus and h is Plank's constant. γ is determined by the unique nuclear structure of each isotope, and is therefore characteristic of that particular isotope.

When placed in a magnetic field B_0, nuclei with a spin I=½ have two energy states, corresponding to their magnetic moments being either parallel to the magnetic field or anti-parallel to the magnetic field. The energy E of each of these states is given by

$$E=-\vec{\mu}\cdot\vec{B_0}=\frac{-\gamma h m B_0}{2\pi}=-\gamma\hbar m B_0 \qquad [2.2]$$

where the quantum number, m, is either ½, for nuclei parallel to B_0, or -½ , for nuclei anti-parallel to B_0. The hydrogen nucleus, i.e. a proton, can have either state, and the two states will be separated by an energy of,

$$\Delta E=E_{1/2}-E_{-1/2}=-\gamma\hbar B_0 \qquad [2.3]$$

The population distribution of the two states is given by Maxwell Boltzmann statistics through the equation,

$$\frac{N_{1/2}}{N_{-1/2}}=e^{\frac{-\Delta E}{kT}} \qquad [2.4]$$

where k is Boltzmann's constant, and T is the temperature in

Kelvin. The observable nuclear magnetic moment (M) of a macroscopic sample is the sum of all the nuclear magnetic moments in that sample. Now to excite the sample the energy applied must excite the nuclei in the lower energy state to the higher energy state. This is accomplished by applying an electromagnetic pulse whose energy exactly matches the energy difference between the two states as expressed in equation 2.3, where ω_0 is the frequency of the electromagnetic wave in that pulse. This energy separation will therefore determine the angular frequency of the pulsed electromagnetic field.

$$\hbar\omega_0 = \Delta E = -\hbar\gamma B_0 \qquad [2.5]$$

Hence to excite the nuclei from one energy state to the other the electromagnetic pulse must have a frequency of $\omega_0/2\pi$, which is called the Larmor frequency.

At a macroscopic level, the behavior of the resultant magnetic moment, $\vec{M}$, of approximately ~10^{26}, nuclei, i.e. roughly Avogadro's number, has many similarities to the laws of classical physics. Since in a magnetic field and at thermal equilibrium more nuclei are parallel to it than anti-parallel, the

equilibrium $\vec{M}=\vec{M}_0$ will be parallel to $\vec{B}_0$. If $\vec{M}_0$ is, as explained later, displaced from its equilibrium orientation, it will experience a torque from its interaction with $\vec{B}_0$ that will, in turn, cause it to precess around $\vec{B}_0$ at it's Larmor frequency ω_0 , see figure 2.1. The variables $\vec{B}_0$ and ω_0 are linked to each other by γ , which is the same for all nuclei of the same isotope. The relationship can be derived from equation 2.5 and is represented in equation 2.6.

$$\omega_0=-\gamma B_0 \qquad [2.6]$$

A convenient simplification for visualizing pulsed NMR is to use, instead of a static frame of reference, one that rotates around $\vec{B}_0$ at the same frequency and sense as the precessing $\vec{M}$. The coordinates in the rotating frame (x',y',z') are such that in both the laboratory frame (x,y,z) and in the rotating frame, the z and z' axis are coincident with each other and defined as parallel to $\vec{B}_0$. This is useful, because when applying an electromagnetic field, $\vec{B}_1$, perpendicular to $\vec{B}_0$ and with a frequency ω_0 , $\vec{B}_1$ will appear to be stationary in

the rotating frame. $\vec{B}_1$ will also exert its own torque on $\vec{M}$ that in turn produces a rotation of $\vec{M}$ about the y' axis by θ degrees as shown in figure 2.2, where,

$$\theta = \gamma \vec{B}_1 t \qquad [2.7]$$

and where t is the length of time the electromagnetic field of strength, $\vec{B}_1$, is applied, i.e. t is the length of the pulse. $\vec{B}_1$ is applied using a radio frequency coil tuned to ω_0. Since, after this excitation pulse, the magnetic moment $\vec{M}$ is no longer parallel to $\vec{B}_0$, but is rotating around $\vec{B}_0$ in the laboratory frame at the Larmor frequency, it will produce it's own electromagnetic field that can be detected using a radio frequency receiver coil tuned to ω_0. This coil can either be the same coil that was used to apply $\vec{B}_1$, or a separate independent receiver coil. The signal detected will be a voltage oscillating at $\omega_0/2\pi$, and orthogonal to $\vec{B}_0$. At the same time as producing the voltage oscillation, the spins are returning to thermal equilibrium. Since fewer of them are contribution to the voltage signal, the signal decreases or decays, as shown in figure

2.3. This decrease in signal is known as a free induction decay or FID. Equation 2.6 which equates the magnetic field strength experienced by the nuclei with the frequency of the nuclear resonance signal can be exploited both for spatial localization in magnetic resonance imaging, and for the identification of chemical compounds in magnetic resonance spectroscopy. It is a very simple yet profoundly far reaching relationship.

2.2.2 Relaxation

Nuclear magnetic resonance experiments begin with the nuclear spin system in thermal equilibrium within itself, and also with its external surroundings. That equilibrium state is destroyed by the electromagnetic pulses that we apply to conduct an experiment. However, the processes of recovery to that overall equilibrium state, provide important information about the interactions that are present in the overall system. Nuclear spins interact both with each other and with other magnetic entities, e.g. electromagnetic fields, within their environment. If these interactions are time dependent, they can promote an exchange of energy, leading to the relaxation of an

excited nuclear spin to its thermal equilibrium state. This is referred to as longitudinal relaxation, because it corresponds to the recovery of the nuclear magnetization parallel to $\vec{B}_0$ i.e., M_z to its equilibrium value M_0 along the direction of $\vec{B}_0$. In the applications described in this thesis, the longitudinal recovery is characterized by an exponential time constant, T_1. After the initial 90° excitation, the nuclear magnetization will also have a transverse component, M_{xy}, in the xy plane, as well as possibly some residual component parallel to $\vec{B}_0$. During the recovery to thermal equilibrium, the transverse, M_{xy}, component usually decays to zero faster than M_z recovers to M_0. The decay of M_{xy} is called transverse relaxation and is characterized by an exponential time constant T_2. It should be remembered at this point that it is the transverse magnetic moment that gives rise to the observable NMR signal, and so it is the time, T_2, which governs how much time we have to observe that signal. The recovery time, T_1, of the longitudinal magnetic moment, M_0, governs how long we have to wait before we can excite the system again to get another maximized M_{xy}. Both T_1 and T_2 are driven, in pure diamagnetic liquids, by the time dependent dipole to dipole interactions between nuclei as they move relative to

each other. The time dependent local dipolar field, $\vec{B}_L$, that is experienced by the nuclei, has a wide frequency spectrum which encompasses frequency components at ω_0 and $2\omega_0$. These are frequencies at which $\vec{B}_L$ is able to change the nuclei's state. The frequency spectrum produced by the random molecular tumbling can be described mathematically by the Debye spectral density $J(\omega)$,where

$$J(\omega)=\frac{\tau_c}{1+\omega^2\tau_c^2} \qquad [2.8]$$

and where τ_c is a correlation time characterizing the random tumbling, which depends on the size and shape of the molecular host and also on the physical state and temperature of the molecular medium. The longitudinal relaxation is optimum when the Debye spectrum for longitudinal relaxation, namely, the components at $J(\omega_{(0)})$, and $J(2\omega_{(0)})$ are maximized. This is the case when

$$\tau_c=\frac{1}{\omega_0} \qquad [2.9]$$

The Fourier components of the spectral density at ω_0 and $2\omega_0$ drive longitudinal relaxation. The transverse relaxation is also driven these components as well as by lower frequency dipolar fields. The effect of these low frequency fields can be visualized causing the transverse magnetic moment $\vec{M}_{xy}$ to fan out in rotating frame space, thereby decreasing the net $\vec{M}_{xy}$. This extra 'decay' mechanism means that T_2 is always shorter than T_1. As mentioned earlier the T_2 relaxation time is also important from a practical point of view, because the longer the signal lasts the more time there is for signal acquisition. The length of the transverse decay can also be reduced by spatial variations in the static magnetic field arising from shortcomings in the NMR equipment or from magnetic susceptibility variations in inhomogeneous samples such as the micro-wires used for ISMS. If this incremental shortening is characterized by the incremental ratio $1/T_2'$, when added to the dipolar decay rate $1/T_2$ will give rise to a composite decay rate that is encountered in practice given by

$$\frac{1}{T_2*}=\frac{1}{T_2}+\frac{1}{T_2'} \qquad [2.10]$$

It is possible to measure just T_2 decay using a spin echo sequence [37,38] which compensates for the $1/T_2'$ as explained later. Excitation and relaxation can be calculated using a family of phenomenological equations postulated by Bloch. First, before considering relaxation, the motion of a magnetic moment, $\vec{M}$, in a magnetic field, $\vec{B}$, is given by the equation

$$\frac{d\vec{M}}{dt} = \gamma \vec{M} \, x \, \vec{B} \qquad [2.11]$$

Where in the NMR context

$$\vec{B} = \vec{B}_0 + \vec{B}_1 = B_1 \cos \Omega t \, \vec{x} - B_1 \sin \Omega t \, \vec{y} + B_0 \vec{z} \qquad [2.12]$$

Equation 2.11 can then be expressed in terms of its Cartesian components, i.e.

$$\frac{dM_x}{dt} = \gamma \left(M_y B_0 + M_z B_1 \sin \Omega t \right) \qquad [2.13]$$

$$\frac{dM_y}{dt} = \gamma (M_z B_1 \cos \Omega t - M_x B_0) \quad [2.14]$$

$$\frac{dM_z}{dt} = -\gamma (M_x B_1 \sin \Omega t + M_y B_1 \cos \Omega t) \quad [2.15]$$

When relaxation is included these component equations become

$$\frac{dM_x}{dt} = \gamma (M_y B_0 + M_z B_1 \sin \Omega t) - \frac{M_x}{T_2} \quad [2.16]$$

$$\frac{dM_y}{dt} = \gamma (M_z B_1 \cos \Omega t - M_x B_0) - \frac{M_y}{T_2} \quad [2.17]$$

$$\frac{dM_z}{dt} = -\gamma (M_x B_1 \sin \Omega t + M_y B_1 \cos \Omega t) - \frac{M_z - M_0}{T_1} \quad [2.18]$$

Equations [2.16] to [2.18] are the phenomenological equations of Bloch.

The three mechanisms of relaxation, T_1, T_2, and T_2^*,

outlined here are highly significant characteristics of magnetic resonance imaging because they represent the cornerstone of the multiple contrast mechanisms that make MRI so powerful as a diagnostic tool.

2.2.3 Magnetic Resonance Imaging

MRI typically and, in the context of this thesis always, is of the hydrogen nuclei, protons, in water molecules. These nuclei are placed in the uniform magnetic field, where since I = 1/2, a Maxwell-Boltzmann distribution of spins between two energy states gives a resultant M_0 parallel to B_0. The coordinate space can be arbitrarily defined as three orthogonal directions p q and r. To localize the response signal in each of these directions linearly varying magnetic fields much weaker than B_0, and called gradients, are applied. The three orthogonal Gradients will enable the total magnetic field to be varied linearly in each of the three orthogonal directions p q and r, in turn. A gradient echo sequence as shown in figure 2.4 is perhaps the simplest imaging sequence but these methods of localization are the same for most sequences.

The first step in an imaging sequence is slice definition. A gradient G_p applied along the p direction will cause the magnetic field B_0 and therefor the potential excitation frequencies to spread out over the range $(\omega_0 \pm \Delta\omega_p)$. The RF excitation pulse with the frequency ω_{ex} anywhere between $(\omega_0 - \Delta\omega_p)$ and $(\omega_0 + \Delta\omega_p)$ is applied. Only nuclei in a slice at field strength $B_{slice} = \omega_{ex}/\gamma$ will be excited resulting in a plane of spins orthogonal to p precessing at ω_{ex} shown in figure 2.5. The nuclei outside this slice will remain in thermal equilibrium, with their magnetic moments parallel to B_0. When G_p is turned off the excited nuclei, and only the excited nuclei will continue to precess but at ω_0.

The second step is phase encoding in which a gradient G_q is applied along the q direction. This gradient will modify both the precession frequency and phase of the nuclei excited in step one. When G_q is turned off the excited nuclei will return to precessing at ω_0 but will retain the phase shift, which they accumulated while G_q was on. Different phases now correspond to different positions along the p direction, as shown in figure 2.6a. When digitalized each strip parallel to r and orthogonal to p and q will have a unique phase.

The third step is frequency encoding. A gradient G_r is applied along the r direction during signal acquisition. This will cause the resonance frequency of the nuclei to vary in the r direction. Again, when digitalized, each section orthogonal to r will have a unique resonance frequency. However, along the length of each section neighboring strips will have different starting phase shifts carried over from phase encoding as shown in figure 2.6.

To extract phase encoding information the sequence is repeated multiple times as G_q is stepped. For each step a position in the q direction will have a different phase as shown in figure 2.6b; these steps can be lined up to create an artificial frequency as shown in figure 2.6c that is unique to each position in the q direction. Applying a two dimensional Fourier transform the time/repetition based data is converted into 2 dimensional frequency based data, and therefore position based points in the q and r directions.

One of the outstanding advantages of MRI is that unlike many other forms of medical imaging, it has multiple methods of contrast. Just as x-ray imaging or CAT scans which use the variations in tissue density, MRI images can reflect the density of

water, in order to provide one contrast mechanism i.e. more water causing a brighter pixel. However the relaxation procedures described in section 2.2.2 can also provide contrast. T_1 contrast is obtained by repeating the excitation sequence before the sample has return to thermal equilibrium, points with shorter T_1 times will appear brighter. T_2* contrast is obtained by delaying the time between excitation of the sample and the acquisition of the FID, giving rise to points with longer T_2* that appear brighter. Using T_2* contrast grey matter appears significantly brighter than white matter. Using a different sequence known as a spin-echo [37,38] where a 180 degree pulse is inserted between a 90 degree excitation pulse and the acquisition it is possible to use T_2 contrast instead of T_2* contrast as the T_2' decay is reversed by the 180° pulse. Other methods are also possible but beyond the scope of this thesis.

2.2.4 Magnetic Resonance Spectroscopy

Water protons are what is looked at in most forms of MRI, but if the signal from water protons is suppressed or otherwise removed (for example by replacing the water with heavy water),

it is possible to observe signals from numerous other biological molecules containing hydrogen nuclei and to identify their relative concentrations. In in-vitro spectroscopy, where NMR was originally developed, the sample can be dehydrated, to remove the H_2O content, and then redissolved in heavy water, D_2O, the signal from which does not interfere with the proton NMR signal from other molecules. Unlike MRI, the magnetic field in an NMR spectroscopy experiment is made as homogeneous as possible, so that details exposed in the NMR signal are the result of properties of the molecules and not of the molecules position in the magnetic field. The two magnetic resonance properties that are used to identify a molecular species are called the chemical shift and the spin-spin coupling, usually referred to as J-coupling, each of which is outlined below.

The chemical shift is a term that describes a magnetic field shift from the externally applied magnetic field that is experienced by a nucleus and is dependent on the intra-molecular environment in which that nucleus sits. That shift is caused by the electronic orbital distribution angular momentum surrounding the nucleus, and which shields the nucleus from the externally applied magnetic field. However, in a manner

reminiscent of electromagnetic induction, the electronic orbital angular momentum readjusts when an external magnetic field is applied, in order to partially screen out that external field from the nuclear site within the electronic shell. The chemical shift, therefore, is dependent on both the applied field and on the electronic configuration of the molecule. The dependence on the electronic configuration enables the chemical shift to be used to differentiate between different molecular species. The chemical shift interaction causes differences of only a few Hz from the resonant frequency of many MHz that an unshielded nucleus would experience in a typical NMR magnet. Because both the nuclear resonance frequency and the chemical shift are linear functions of the applied magnetic field, to make spectral comparison between magnets easier, the chemical shift is normally quoted in parts per million of the applied field, ppm, a unit-less measure that is independent of the magnetic field strength. Equation 2.19 calculates ppm where f_{ref} is the reference frequency of an “unshielded” nucleus and f_{sample} is the frequency of the target nucleus in a specific molecule.

$$ppm = \frac{(f_{(ref)} - f_{(sample)}) \times 10^{(6)}}{f_{(ref)}} \qquad [2.19]$$

As the ppm measure is independent of field strength it is possible to use previous studies [39] that looked at a molecule of a particular structure to identify that same molecule in an unknown solution. When performing these experiments in-vitro the reference frequency is, by convention, defined from a standard H_2O solution of DSS (4,4-dimethyl-4-silapentane-sulfonic acid) and is typically provided by adding DSS to the sample solution**.** The singlet resonance line from the DSS can provide both a marker for 0 ppm and also an absolute concentration measure. In in-vivo NMR however the reference frequency has to be determined from the rf receiver system and, moreover, it is only possible to determine the relative concentrations for biological molecules.

J-coupling arises because nuclear spins and electron spins are both endowed with magnetic moments, which enables them to interact with each other. The electron bonding orbitals in a molecule (which can communicate this nuclear spin information) extend though space linking the sites of at least two nuclei in

that molecule. For example if the magnetic moment of a nucleus N_1 is, say, parallel to B_0, then the electron orbitals surrounding N_1 will have a propensity for their net spin density to be anti-parallel to B_0. If the atom containing N_1 is bonded to a neighboring atom with nucleus N_2, the bonding orbitals between the two atoms overlap and because of Pauli's Exclusion Principle, the bonding orbital electrons on the atom containing N_2 will have a propensity to be parallel to B_0. The nucleus N_2, as always, can be either parallel or anti-parallel to the field B_0. However, because of its interaction with the bonding orbitals of its parent atom that, in the situation described, have their electronic spins preferentially parallel to B_0, the nucleus N_2 will have both of its two energy states shifted slightly. The direction of that shift will depend on whether the spin of N_2 it is parallel or anti-parallel to the electronic spin density. As a result, the energy/frequency of a nuclear transition will be either increased or decreased slightly, and the resulting spectrum is now a doublet not a single resonance line.

The example of acetaldehyde CH_3CHO, as shown in figure 2.8 is an illustration of this. In this molecule the three methyl group protons are equivalent and as such they will behave

similarly. As a group they are bonded to the aldehyde proton though three bonds i.e. (H_3-C-C-H). The three CH_3 protons will be affected similarly by the aldehyde proton spin into two possible orientations. The energy states of each methyl proton will therefore develop two corresponding pairs of energy states, depending on the aldehyde proton being either parallel or anti-parallel orientation of B_0. The resulting spectrum is shown in figure 2.8a.

The aldehyde proton however, will be affected by all three methyl group spins. There are four different combinations of the three spins, all parallel, two parallel one anti-parallel, one parallel and two anti-parallel, or all anti-parallel, so the aldehyde protons signal is split into a quartet. The tree diagram in figure 2.8b illustrates that the middle two options are three times as likely as the two edge options, and therefore are three times as strong resulting in a 1,3,3,1 spectrum as shown in figure 2.8b.

Precession Cone of a Nuclear Magnet

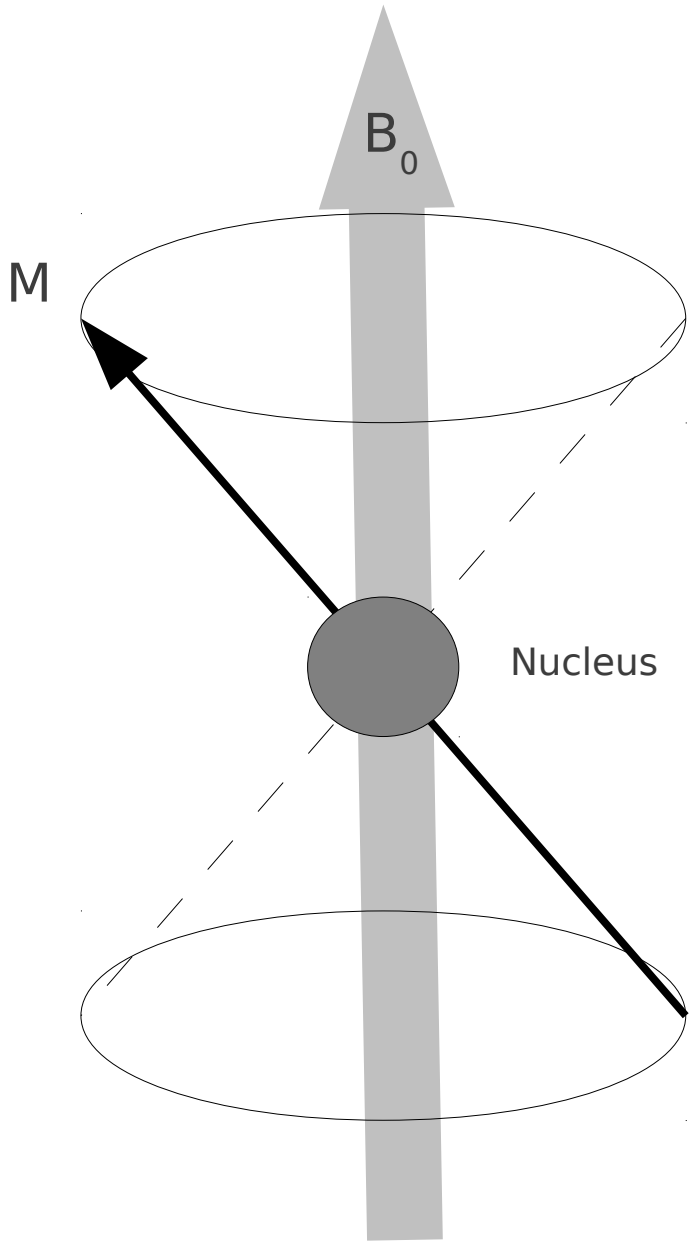

Figure 2.1 A proton nucleus, magnetic moment M, precessing in a magnetic field B_0.

Rotating Frame of Reference Representation of NMR

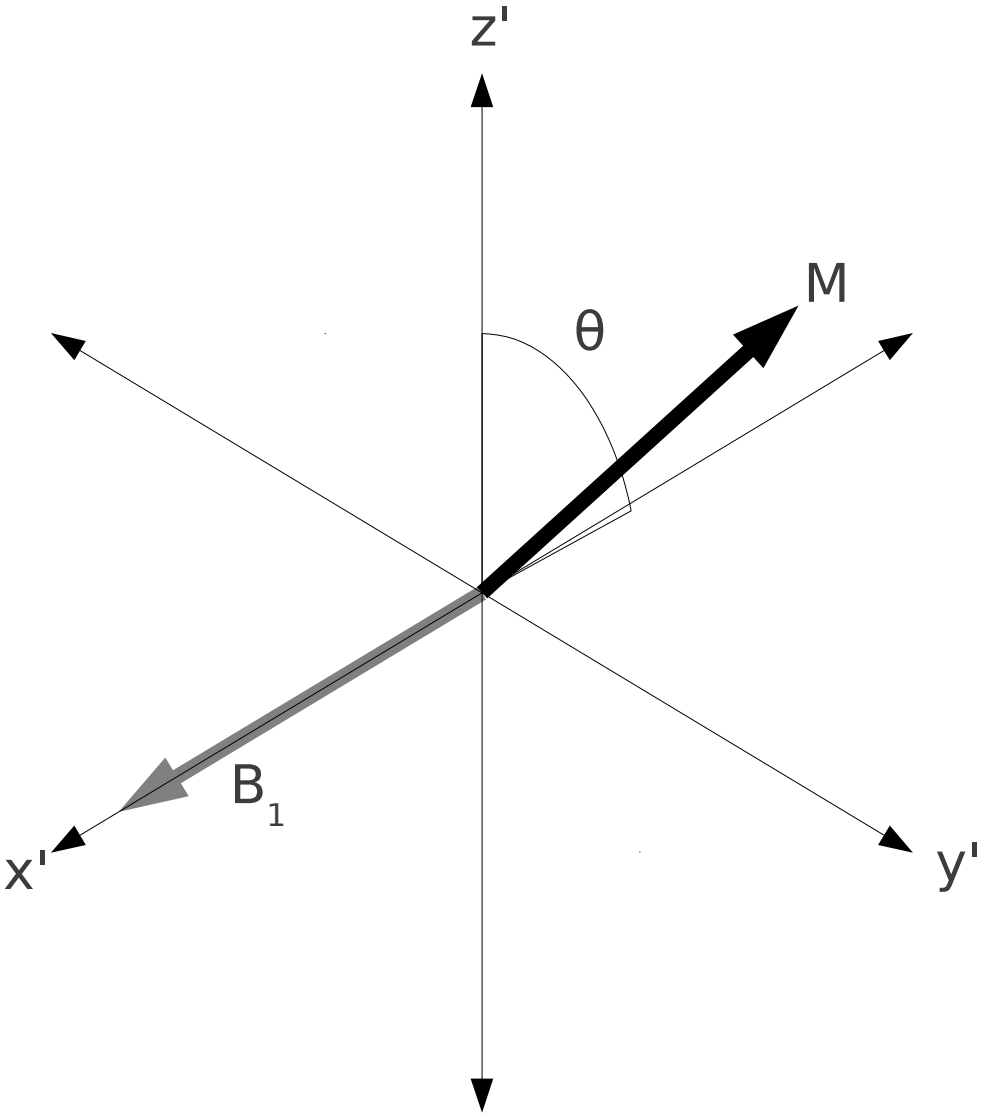

Figure 2.2 Excitation of a magnetic moment M by an applied field B_1 though flip angle θ in a rotating reference frame, x', y', z'.

Free Induction Decay of the Nuclear Signal

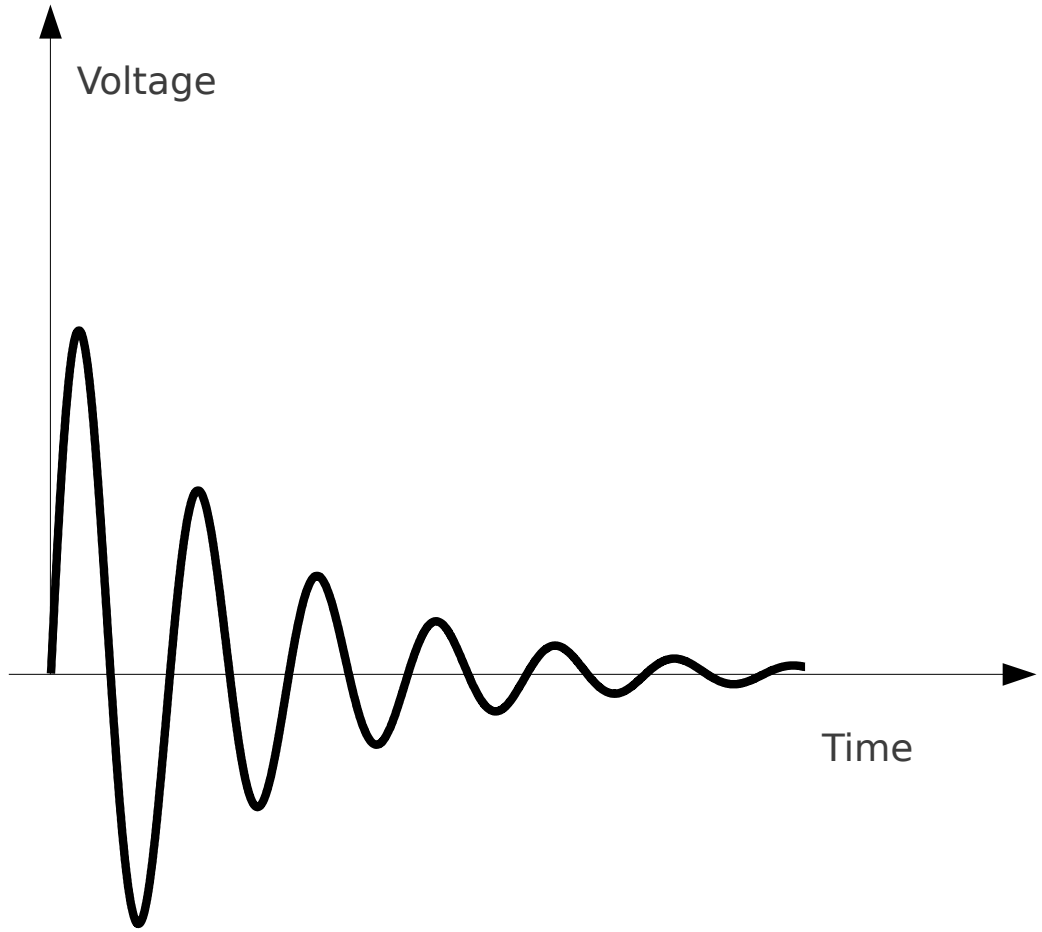

Figure 2.3 The exponential decay of the sinusoidal signal produced by an excited nucleus in a magnetic field.

Gradient Echo Imaging Pulse Sequence

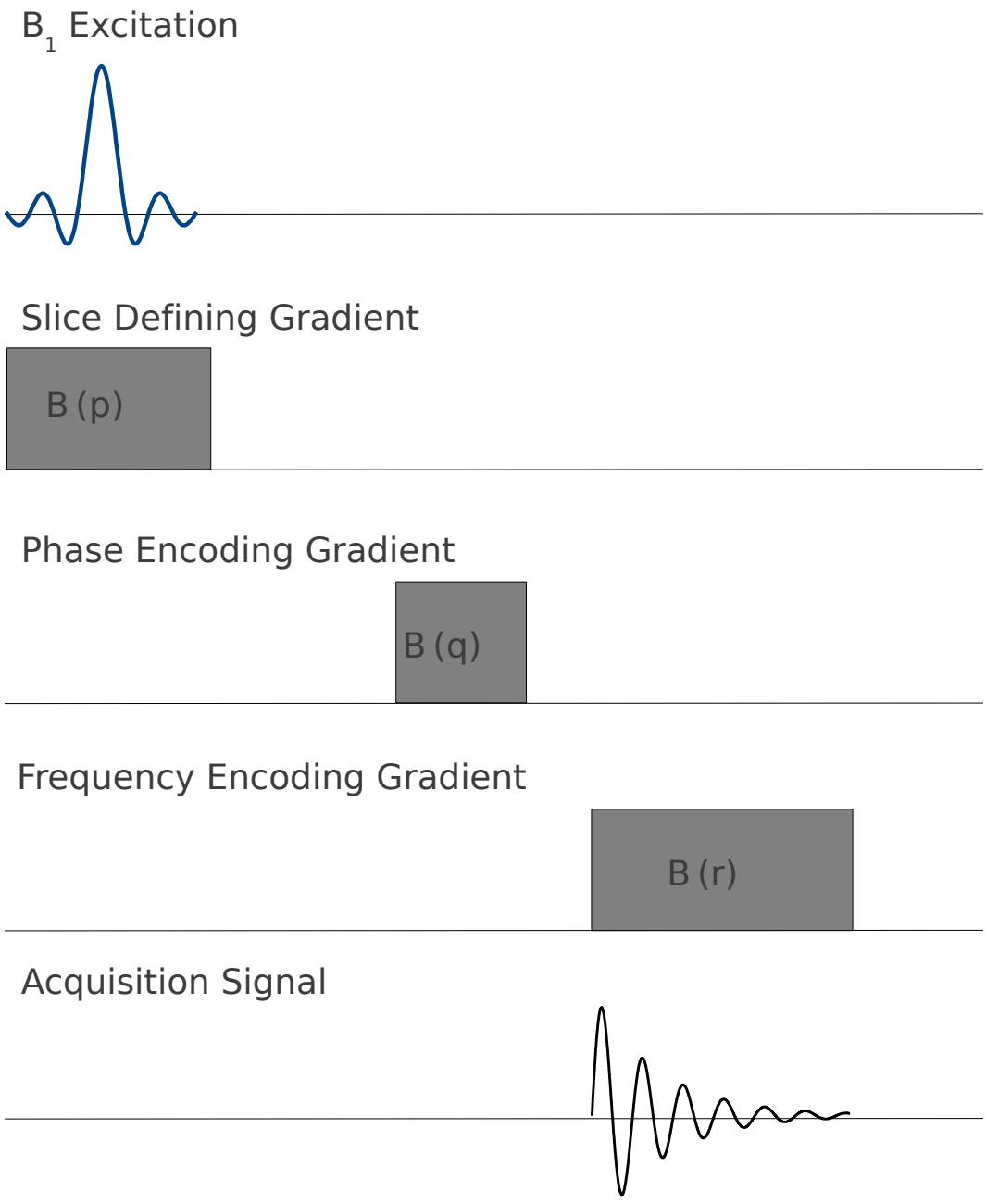

Figure 2.4 A Gradient Echo pulse sequence showing excitation gradients and signal acquisition.

Slice Selection

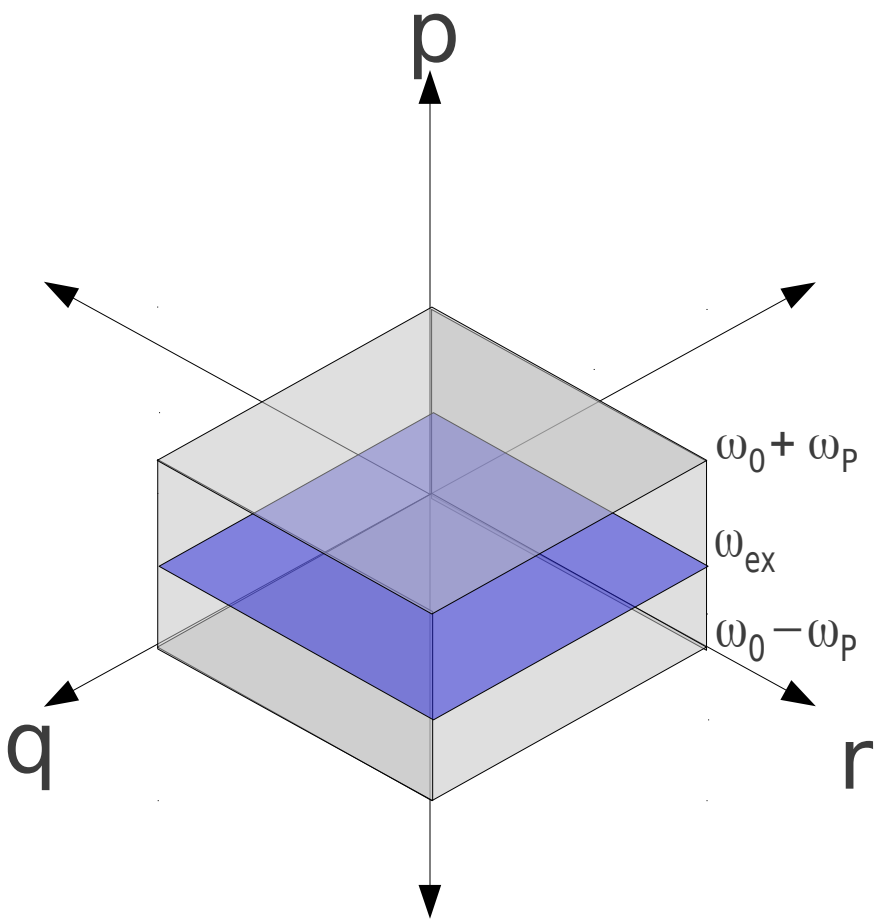

Figure 2.5 Slice selection from a cube, in light grey, of a plane, blue, in the q direction. The magnet frequency ω_0 is spread out from $\omega_0 + \omega_p$ to $\omega_0 - \omega_p$, the excitation frequency, ω_{ex}, is between these limits.

Spatial Phase Encoding

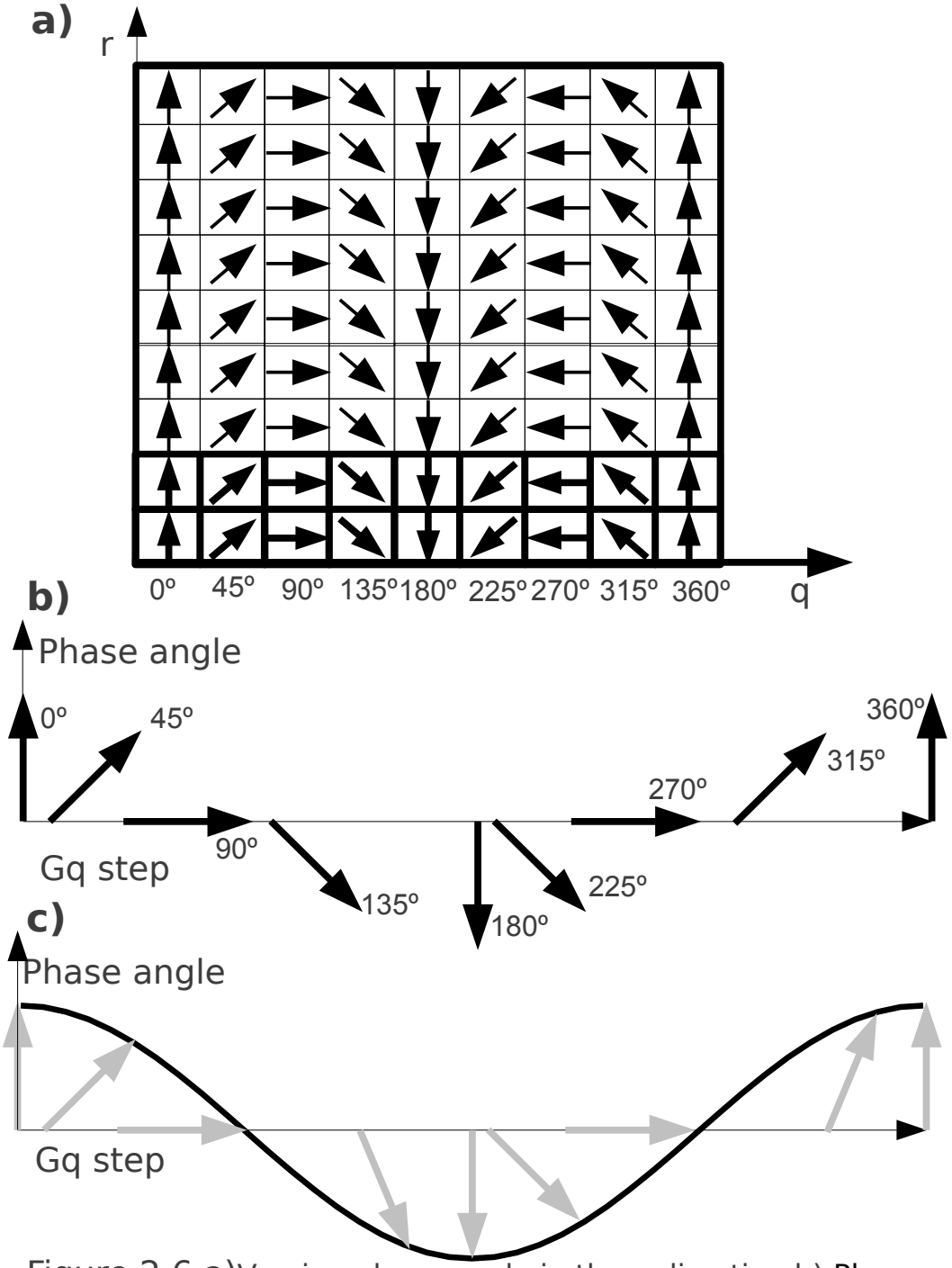

Figure 2.6 a)Varying phase angle in the q direction b) Phase angle steps with varying gradients in the q direction
c) Constructing phase angle into artificial frequency

Phase and Frequncy Encoding of a Slice

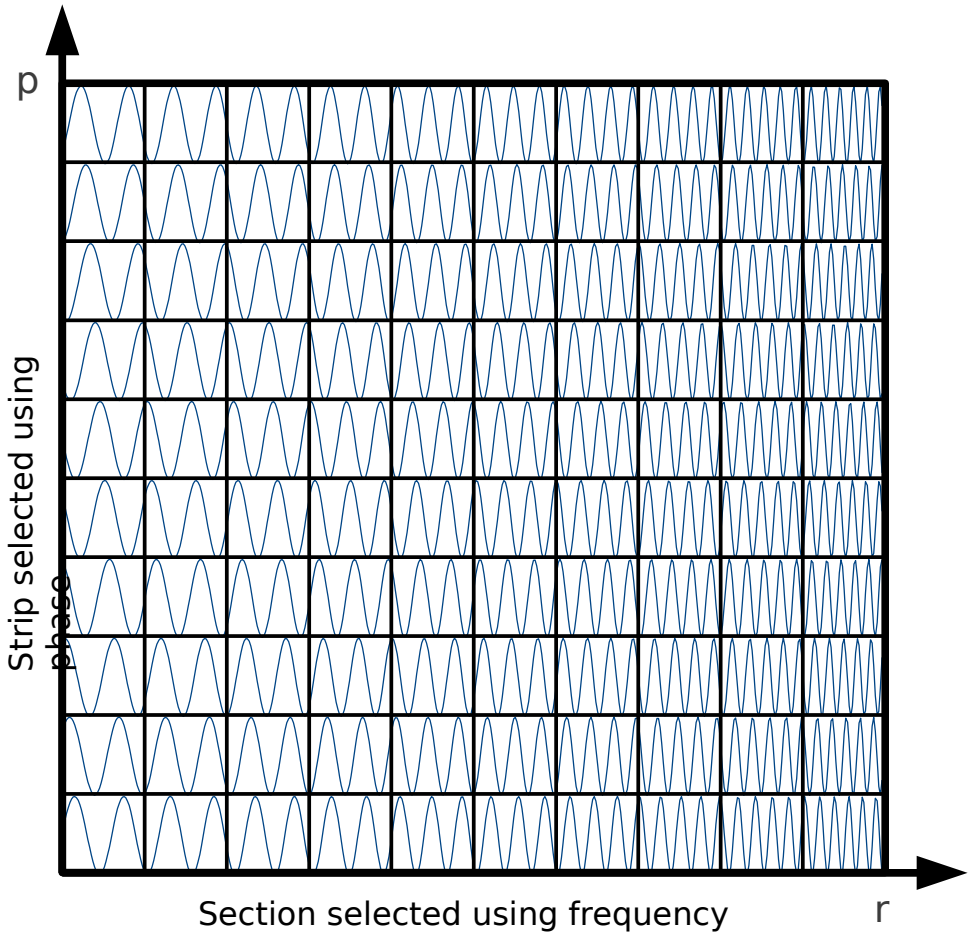

Figure 2.7 The phase encoding gradient in the p direction separates the excited slice into strips each with its own unique phase. Then the read encoding gradient separates each strip into separate secions based on their frequency.
.

Spectral Effects of Internuclear J-Coupling

CH_3CHO

a)

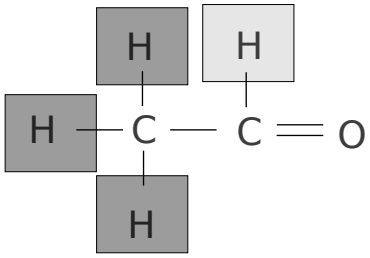

Protons producing signal
J-Coupled proton

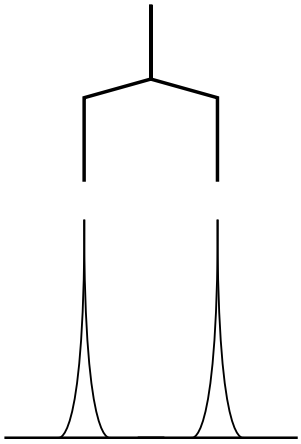

Resulting signal

b)

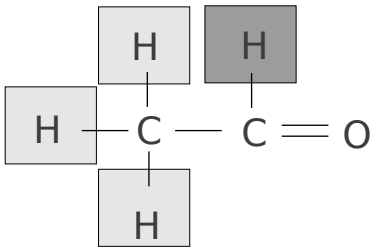

Proton producing signal
J-Coupled protons

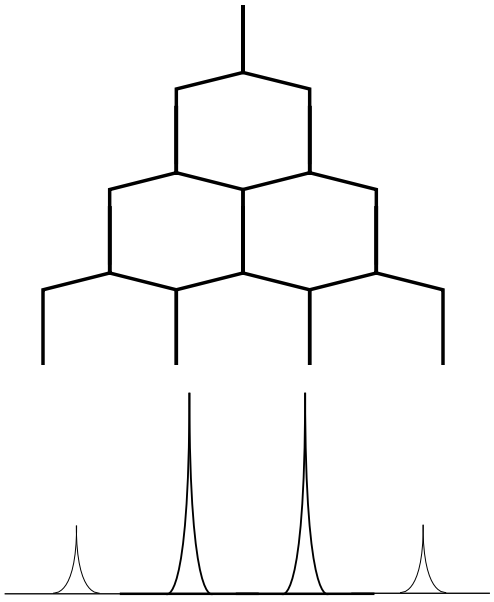

Resulting signal

Figure 2.8 a) Signal of three protons coupled to one proton
b) Signal of one proton coupled to three protons

3. Methods

The experimental work described in this thesis can be divided into 4 sections. The first uses MRI to enable visualization of the spinal cord and micro-wires used for ISMS. The second exploits transverse nuclear magnetic relaxation (T_2), contrast in the images in order to monitor the spatial distribution of water relative to a spinal cord injury. The third employs in-vitro MRS, in order to evaluate metabolite changes in spinal sections relative to their distance from an injury. Finally, in-vivo MRS is explored for evaluating its non-invasive analytical capability of key metabolites.

3.1 Imaging

Imaging was conducted using a 3 Tesla, 127 MHz, clinical 1 meter bore magnet (Magnex Scientific, SMIS console, Edmonton, Alberta). A cat animal model was used. The purpose for this was to evaluate the efficacy of using MRI to provide pre-operative coordinate information for the placement of micro-wires in the spinal cord of a cat for ISMS applications, and subsequently to

locate these wires post-operatively. Because the magnet is used for human studies as well as animal research it was necessary to create a customized container for the cat to prevent contamination of the magnet. This container was made out of Plexiglas. In addition, a specifically tailored radio frequency (RF) imaging surface coil was constructed of copper tape on a thin plastic mold and integrated into the Plexiglas container. This provided a small coil, 16 cm long by 8 cm wide, located immediately adjacent to the spinal cord. The size matching of the coil to the cat provided the best signal to noise ratio and hence the best possible image.

To achieve optimal RF transmission and reception the RF coil should resonate at the proton Larmor frequency at 3T. A coil's resonant frequency, ω, is determined by

$$\omega = \frac{1}{\sqrt{LC}} \qquad [3.1]$$

where L is the inductance of the coil and C is its capacitance. The inductance is provided by the self-inductance of the strips of copper tape forming the coil, gaps are then cut into the coil and bridged with capacitors, as shown in figure 3.1a, to satisfy

equation 3.1. The inductance of the coil is also be affected by the impedance properties of the sample placed within it. To compensate for this, a variable tuning capacitor is placed in parallel with the capacitor bridging the input gap. The tuning capacitor's capacitance can be easily varied so that the total capacitance of the coil satisfies equation 3.1 for a range of possible inductances created by various samples. To maximize signal transfer, the RF impedance of the coil should match the characteristic impedance of the cables transferring the RF pulses from the pulse generator to the coil and subsequently the coil to the receiver. This can be done by placing a variable capacitor in series with the cable between the coil and the receiver as also shown in figure 3.1a, an image of the coil is shown in figure 3.1b.

The initial imaging of the spinal cord was performed in-vivo with a gradient echo pulse sequence ([40] and figure 2.6), with an echo time (TE) of 25 ms, a repetition time (TR) of 850 ms, and the flip angle was the Ernst angle. Echo time (TE) is the time between excitation and acquisition, TR is the time between excitations, flip angle (i.e. the angle though which the the equilibrium magnetization is nutated) reflects the strength of the excitation pulse. The Ernst angle [46] is the compromise

excitation pulse nutation to maximize signal to noise obtainable within given time parameters. It is obtained by varying the strength of the excitation pulse while maintaining the parameters of position and time to obtain the strongest signal. Phase encoding was in the horizontal plane to minimize breathing artifacts. Slice thickness was 4 mm and a field of view of 160x160 mm with 512x512 pixels resulted in an in-plane resolution 0.31 mm/pixel.

Imaging the micro-wires was conducted in-vitro on extracted spinal cords. A spin-echo sequence was used as it is less susceptible to the distortions caused by the micro-wires. The micro-wires used for ISMS were 30 micron in diameter and made of either stainless steel or 80/20 platinum/iridium alloy. For MRI purposes, platinum/iridium alloy is preferred because stainless steel experiences significant forces inside the magnet due to its greater magnetic susceptibility. Moreover, greater image artifacts are also produced by stainless steel of the same size because of its greater conductivity, which gives rise to larger eddy currents, and its magnetic susceptibility. The parameters used were TE 34 ms, TR 2000 ms. Slice thickness was 1.5 mm, a field of view of 100x100 mm over 256x256 pixels resulted in an

in-plane resolution of 0.39 mm/pixel.

3.2 Water Compartmentalization

Proton T_2 relaxation provides contrast in spin-echo imaging and represents the exponential rate of signal decay in a spin-echo sequence. It can also be used to investigate sub-pixel structural changes. By collecting images with different spin-echo times a decay curve can be constructed for a pixel or group of pixels. The decay curve can then be compartmentalized into water in myelin and water in other cellular structures as well as the extracellular environment. Initially, using the surface coil designed for in-vivo imaging of the spinal cord in the 3T magnet, a series of transverse spin-echo images (a spin echo sequence is illustrated in figure 3.2), were acquired with 13 echo times ranging from 7 ms to 600 ms. Each image had a TR of 2s, field of view of 120 mm, 3 mm slice thickness, and 256x256 acquisition matrix. This procedure was performed on both a control cat and a cat with a complete transection at T11. Relaxation measurements (T_2) were made at five locations along the spinal cord, namely, 10 mm rostral to the lesion, the lesion site at T11,

and 12mm, 21mm, and 35mm caudal to the lesion site. Using a non-negative least squares methodology [42], average transverse relaxation rates were obtained for four pixel volumes, both in gray and in white matter at each of these five locations. This method is susceptible to any subject movement that occurs between image acquisitions; and to any imperfections in the 180 and 90 degree pulses delivered from the surface coil. This surface coil B1 inhomogeneity arises because the power of the B1 field decreases as a function of distance from the coil.

A volume coil which produces a relatively, spatially uniform B1 field can mitigate the pulse imperfections, but suffers from a lower signal to noise ratio than the tighter coupling surface coil. It is however possible to get the best of both worlds, i.e., the B1 homogeneity of the volume coil while still maintaining the advantageous signal to noise ratio of the surface coil. This was done using a Transmit Only Receive Only (TORO) coil system to exploit the benefits of both coil types. The surface coil receiver used was the same as mentioned in the imaging section but, with additional decoupling circuitry. The volume transmission coil was constructed as a 28 cm diameter, 16 element bird-cage coil. The coils were passively decoupled using crossed diodes. The diodes

were forward biased by the high power of the transmit pulse, but reverse biased during the lower power of the received signal.

To reduce movement artifacts, instead of using a series of spin-echo images with different echo times, a Carr-Purcell-Meiboom-Gill (CPMG) [38,41] sequence was modified to collect images. A traditional CPMG sequence is a 90 degree excitation pulse followed by alternating read periods interspersed with 180 degree refocusing pulses (figure 3.3). To collect an image, slice select, phase and frequency encoding gradients are incorporated into the CPMG sequence, as shown in figure 3.4, so that a series of images for the same slice but with increasing echo times can be collected. The procedure can then be repeated for different slice selections. This procedure reduces the severity of movement artifacts that would arise from collecting several sets of single spin echo images. The modified CPMG sequence was used to acquire images with effective echo times at 7 ms, 8 ms, 10 ms, 15 ms, 30 ms, 50 ms, 80 ms, 100 ms, 125 ms, 150 ms, 200 ms, and 300 ms, with a TR of 2s, field of view of 120 mm, 3 mm slice thickness, and 256x256 acquisition matrix. The images were collected at the same 5 positions with respect to the lesion as the spin-echo images. Using non-negative least squares [42],

relaxation rates were obtained for four pixel averages in gray and in white matter at all five sites.

3.3 Magnetic Resonance Spectroscopy

3.3.1 In-vitro Spectroscopy

Using in-vitro MRS, it is possible to distinguish and to observe biological molecules with greater precision than it is possible in-vivo. This is the result of several factors, namely, (a) the availability of much higher magnet strengths albeit at narrower bore diameters, 18.8 T as opposed to 4.7 T, thereby separating the signals from different metabolites over a larger bandwidth; (b) the replacement of water with heavy water as the solvent thereby attenuating the contaminating water signal; (c) the addition of DSS, 4,4-dimethyl-2-silapentane-5-sulfonic acid, as an absolute reference of both frequency and proton concentration; and (d) the more uniform magnetic field across the sample also made possible by the smaller magnet bore and the uniform nature of the sample. In-vitro MRS can be used to look a broad range of biological molecules and identify changes

that can be observed in-vivo.

This part of the work was conducted using a rat model. There were 6 rats in each of the following groups, control, 4 hours, 1 day, 1 week, and 4 weeks after spinal cord injury. The experimental rats were anesthetized and their spinal cords exposed by a laminectomy at the thoracic level (T8). To replicate a severe injury, a custom clip was used to apply a pressure of 7 mm Hg across a 2 mm length of the spinal cord at the T8 level for 60 seconds. The rats received 0.05 mg/kg of buprenorphine immediately after surgery for pain control and 5% Trimel in their drinking water to prevent infection. In addition, the rats received muscle stretching and bladder expression twice daily to mitigate other complications such as spasticity.

To extract the spinal cords, the rats were placed under isoflurane at 4 hours, 1 day, 1 week, or 4 weeks after injury, the control group was also placed under isoflurane for spinal cord extraction. Once anesthetized, the rats received a complete laminectomy to expose the spinal cord and the ventral and dorsal roots were cut. The spinal cords were then extracted, placed on a cold block and cut into equal rostral, lesion, and caudal sections, each approximately 2cm long and with the site

of the initial injury at T8 at the center of the lesion section. Within 10 minutes of extraction, the sections were frozen in liquid nitrogen and ice cold isopentate for 2 minutes and stored at -80°C to limit chemical changes after removal.

The samples were prepared with a modified version [43] of the total lipid extraction method [44]. Samples were initially homogenized in 2.66 mL methanol and 1.33 mL chloroform for each gram of tissue. The samples were homogenized a second time with 1.33 mL chloroform, and finally with 1.33 HPLC grade water. Of the resulting homogenate 0.75 mL was extracted and centrifuged at 2000 rpm for 15 minutes. From the methanol layer 0.2 mL was extracted and kept at -20 °C overnight then dried in a savant for 2 hour before being returned to -20 °C. The samples were reconstituted using 0.6mL of distilled water, 0.06 L of heavy water, 100 mm imidazole to indicate pH, 0.2% NaN_3 to inhibit bacterial growth and 5mM DSS as a reference for both frequency and concentration.

Each sample was then evaluated on a 800Mz Varian spectrometer at 25 °C. After saturating the water signal with a 90° pulse-acquire, the 1H spectrum was acquired with a 4s acquisition time, and a 11.99 MHz sweep for 32 averages. The

resulting spectra were analyzed with the proprietary Chenomex profiling software that fits the experimental spectrum to a library of spectra of known biological molecules. Concentrations were determined from the area under the peaks, by comparison with the DSS peak area in each sample. The molecules fitted were glutamate, glutamine, N-acetylaspartate (NAA), N-asetylaspartateglutamate (NAAG), GABA, myo-inositol, glycine, glycerol, choline, and creatine. Mono-amine neurotransmitters were not included despite their involvement in spinal cord injury [45] because their concentrations would be lower than that which could be detected by in-vivo MRS. Creatine and phosphocreatine were measured together as total creatine because of their similar structures (figure 3.5). Their primary resonance differ by only 0.002 ppm [39], which is indistinguishable even at 800MHz. Phosphocreatine does have a unique resonance at 7.29 ppm [39] but this is beyond the bandwidth of most in-vivo scanners. Another possible method of measuring phosphocreatine would be to use phosphorus spectroscopy. Choline, phosphorylcholine, and glycerophosphocholine are similarly measured as total choline, again due to their similar structure, (figure 3.6). This results in

their primary resonance differing by less than 0.027 ppm [39]. Although they could have been measured separately in-vitro, they would be indistinguishable in-vivo. The additional unique resonances in both phosphorylcholine and glycerophosphocholine are from only one or two protons in contrast to the nine protons contributing to the primary resonance. They are therefore considerably weaker and difficult to detect.

The mean concentrations of all metabolites from the injured animals were then normalized to the mean concentrations of the control animals at the same location. Temporal comparison was done for each normalized time point after injury with the control concentration at the corresponding location. Spatial comparison was done between the normalized mean values of each spinal cord location for a given time point. Both temporal and spatial comparisons were made using independent sample t-tests with $\alpha=0.05$.

3.3.2 In-vivo Spectroscopy

The eventual goal of MRS is to be able to perform this type of analysis non-invasively and in-vivo. To look at the feasibility of

this in-vivo MRS a test was conducted in an adult anesthetized cat using a 3 Tesla, 127 MHz, clinical sized magnet using the same surface coil used for imaging. Selecting a 5x5x20 mm volume in the feline lumbar enlargement and using CHESS water suppression an in-vivo sample spectrum was collected showing NAA, creatine, and choline peaks, demonstrating that it is possible to measure retaliative concentrations of these three metabolites in-vivo.

A Surface Coil

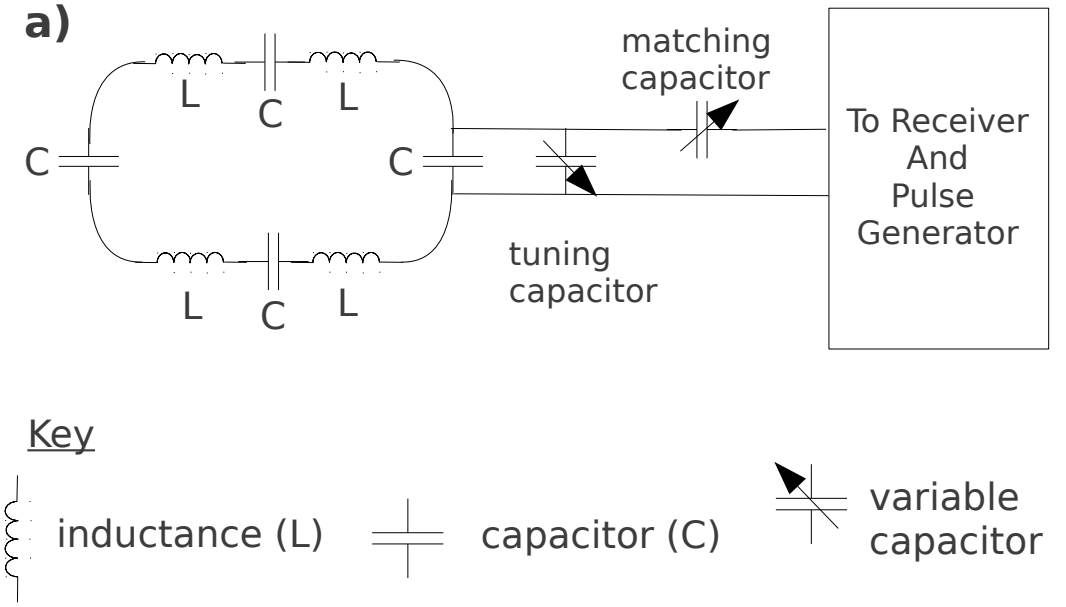

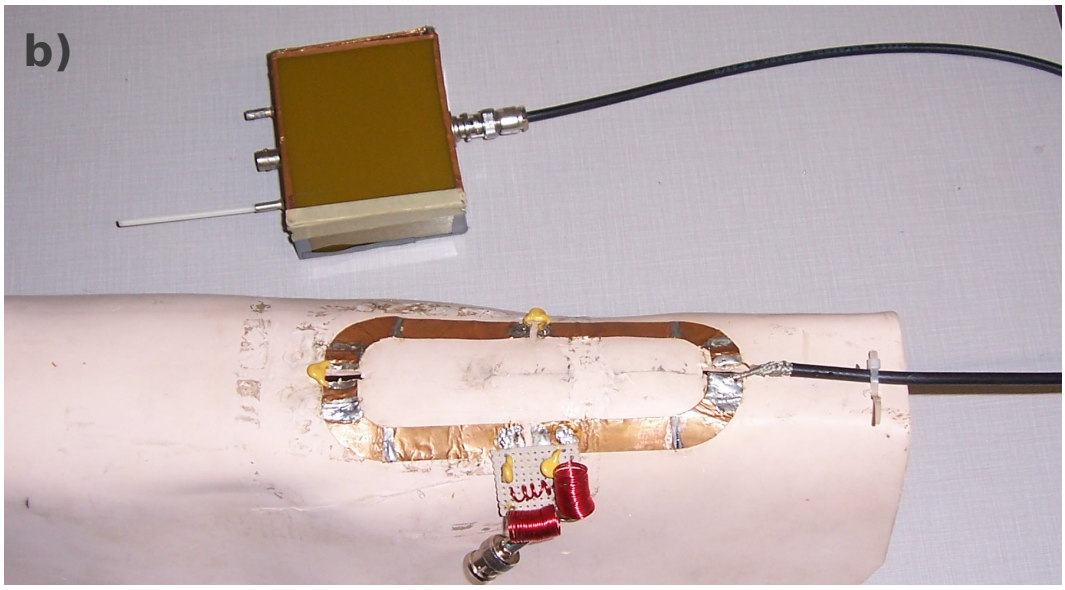

Figure 3.1 a) Electrical schematic of a surface coil b) Image of a 16 cm by 8 cm surface coil. The matching and tuning capacitors are in the box, the extra circutry on the bottom is for decoupling.

Spin Echo Imaging Sequence

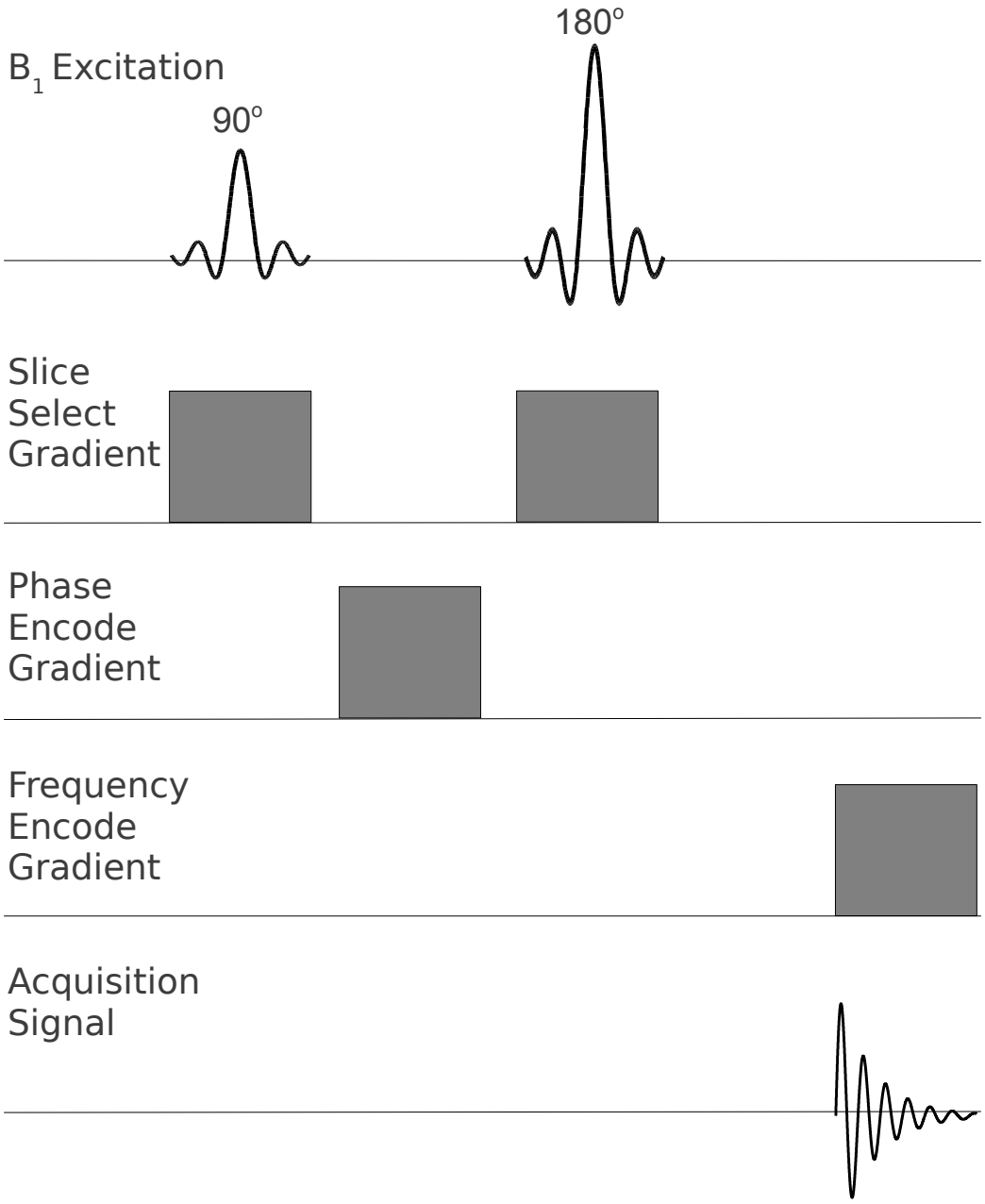

Figure 3.2 A Spin Echo pulse sequence showing excitation gradients and signal acquisition, time scale is in ms.

Conventional CPMG Sequence

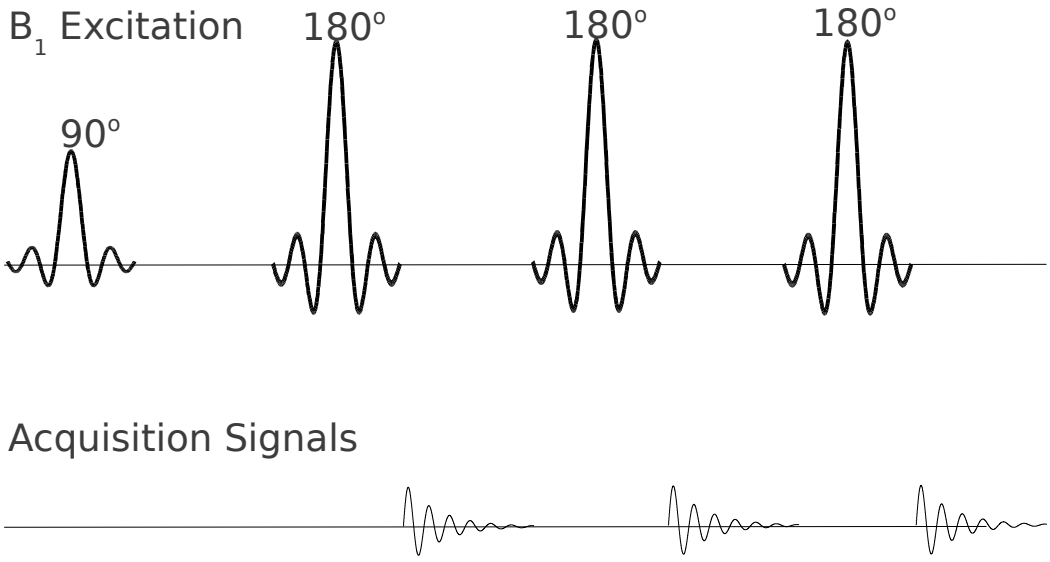

Figure 3.3 Excitation and acquisition signals in a Carr-Purcell Melboom-Gill pulse sequence, time scale is in ms.

CPMG Imaging Sequence

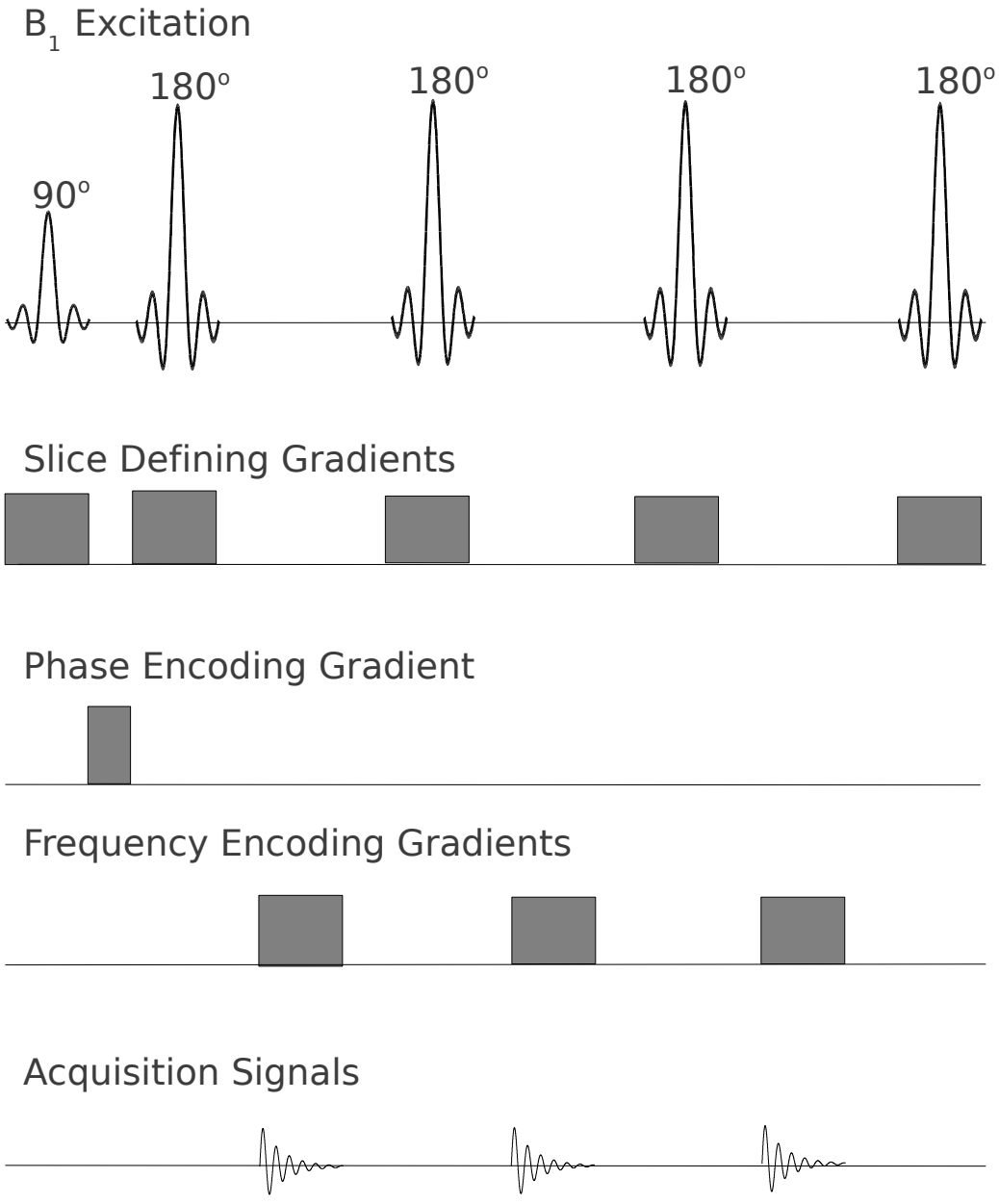

Figure 3.4 A CPMG sequence excitation and acquisition pulses modified with gradients to produce a series of spin echo images, time scales are in ms.

a) Creatine

$OOC.CH_2.N(CH_3).C(NH)NH_2$

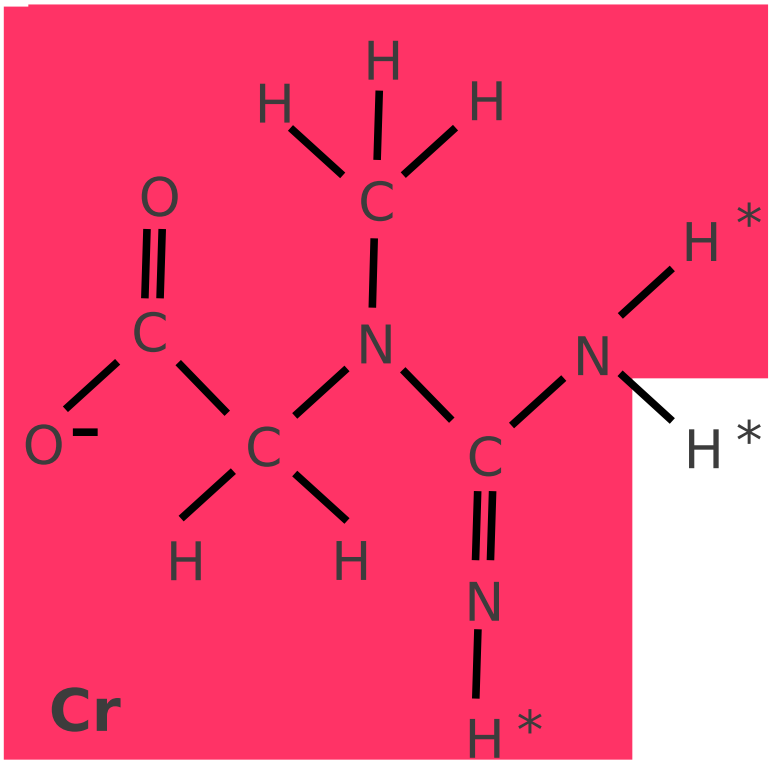

* indicates exchangeable protons

b) Phosphocreatine

$OOC.CH_2.N(CH_3).C(NH)NH.PO_3$

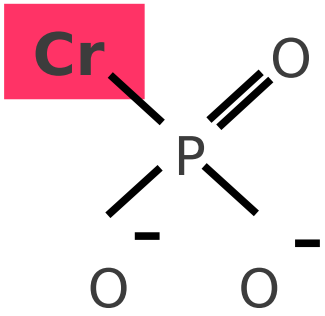

Figure 3.5 a) The chemical structures of creatine b) The chemical structure of phosphocreatine

a) Choline

$(CH_3)_3NCH_2CH_2OH$

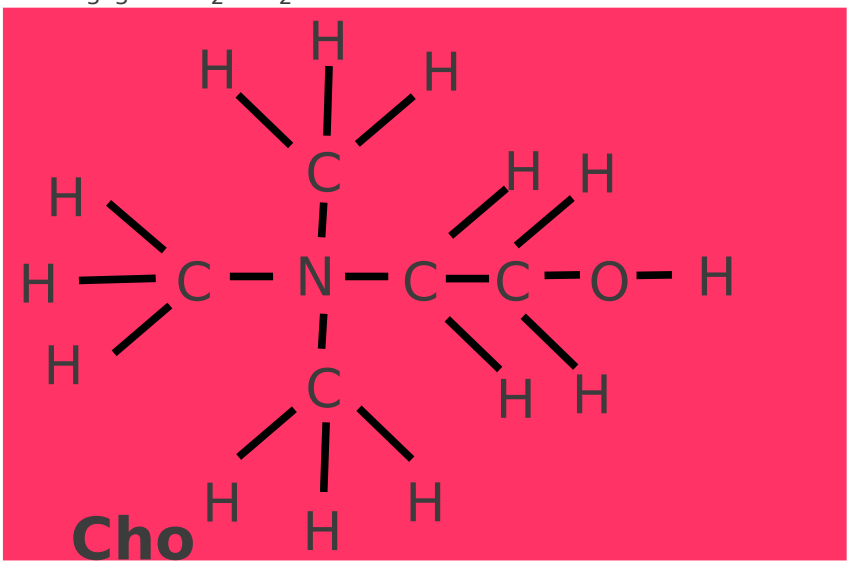

b) Phosphorylocholine

$(CH_3)_3NCH_2CH_2OPO_3H$

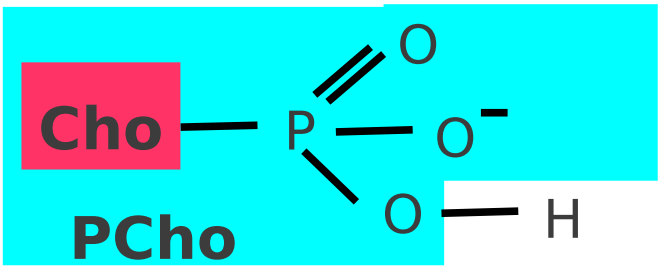

c) Glycerophosphorylcholine

$(CH_3)_3NCH_2CH_2OPO_3CH_2.CHOH.CH_2.OH$

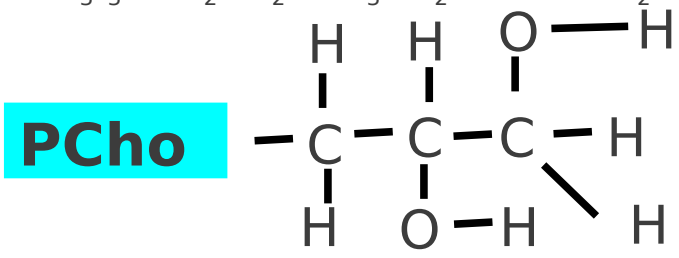

Figure 3.6 a) The chemical structures of choline b) The chemical structure of phosphorylocholine c) The chemical structure of glycerophosphorylcholine

4. Results and Discussion

4.1 Imaging

There were three objectives to imaging the spinal cord. First, imaging actual lesions or other damage; secondly, providing pre-operative images of the spinal cord for use with intra-spinal stimulation; and thirdly, imaging the micro-wires used in intra-spinal micro-stimulation to establish exactly where they have been implanted. Typical pre-operative images of the spinal cord, as acquired using gradient-echo imaging, are shown in figure 4.1 as a transverse image, in 4.2 as a coronal image, and 4.3 as a sagittal image. All three of these images have a 0.35 mm in plane resolution and a 4 mm through plane resolution.

The wire images in figure 4.4 were acquired from an excised feline spinal cord that had previously had a Pl-Ir array of micro-wires implanted. The cord was placed in a water filled test tube. This image is a spin echo image, 0.39 mm in plane resolution, 1.3 mm though plane resolution. Figure 4.4a comprises two transverse sections; 4.4b is a coronal image of the array; and 4.4c is a sagittal section image. Of particular note is

that in both 4.4a and 4.4c, the micro-wires are not vertical but deviate up to 45 degrees. These images show that the signal voids caused by the micro-wires are large enough to show up in the image but not so large as to obscure the image of the spinal cord. The imaging of the perfused but undissected spinal cords with their micro-wire array shows the physical position of the wires and can be used to better understand the position of physiological regions used in ISMS. These images also led to changes to micro-wire implantation procedure to ensure that the are being implanted vertically. The next step would be to image the micro-wire array in-vivo to further advance our understanding of these regions. This understanding coupled with the detailed pre-operative images and new implantation procedure would allow pre-operative planning of ISMS for a specific patient and increase the accuracy of micro-wire positioning intra-operatively.

4.2 Water Compartmentalization

Transverse relaxation (often quantified by the exponent measure T_2) gives rise to one form of contrast used in imaging. By taking a series of images with a succession of increasing echo

times, any actual non-exponential decay can be broken down into its separate exponential components that in turn provide information about the cellular structure in the spinal cord. In figure 4.5a for example, a diagram of the spinal cord shows the two regions, grey and white matter, for which sample T_2 distributions were calculated. In figure 4.5b a typical decay curve from multiple echo times is shown, and finally in figure 4.5c the exponential component T_2 distributions are displayed. Previous studies on excised nerve tissue, carried out on animal-size MR systems [47,48] have reported four transverse relaxation components in white matter and two components in gray matter. The shortest T_2 component, previously observed in either gray or white matter, occurs near T_2 = 1 ms and was identified as originating from protons in phospholipids [48]. It is however beyond the technical capabilities of the equipment available for this study. The shortest echo time within the capacity of our human-size MR units is 7 ms, so it is unsurprising that any 1 ms T_2 component was not seen in our work. A second component reported in the previous studies occurs in a range of T_2 between 10 ms and 20 ms and was reported only in white matter. The T_2 component between 10 ms and 20 ms was identified as the

hydration water between individual myelin layers [48]. In our study such a white matter component was observed, and it comprised 25 to 45% of the white matter signal (figure 4.5c). The third and largest T_2 component reported in the previous studies occurred between T_2 values 50 ms and 100 ms, and, moreover, it was reported in both white matter and gray matter. This largest T_2 component was previously assigned to both axonal and extracellular water. In our study a T_2 component between 50 ms and 100 ms was observed in both gray matter and white matter. In white matter this 50 ms to 100 ms T_2 component comprised over 50% of the T_2 decay curve (figure 4.5c). The final component reported in the white matter of previous in-vitro studies [48] but not seen in our work, was a small T_2 component with a long relaxation time greater than 120 ms. It is possible that in our study this component was to small to be detectable with available hardware. This project demonstrated that it is possible to measure some T_2 components in-vivo in a sample as small as the gray matter or white matter of the lumbar spinal cord in a cat. These components may vary due to injury or possibly due to position in the spinal cord as observed in figure 4.6. The axonal and extracellular T_2 values

trend longer as we progress down the cord rostral to caudal perhaps indicating less structure. This could be a function of the injury, because the caudal sections are further from the lesion. However, it will require the measurement of T_2 distributions from healthy animals to resolve this. After that, histology will be needed to determine the cause of the T_2 changes. One possible explanation would be that the increases in water mobility are a function of inflammation.

4.3 In-Vitro MR Spectroscopy

Neurological injury is known to cause neurochemical changes. For example, traumatic brain injury causes an excessive release of excitatory amino acids [49]. Studies have also been done on the spinal cord. Other factors such age, inflammation, edema, ischemia, and free radical production are all expected to cause chemical changes in the spinal cord. Magnetic resonance spectroscopy has two major advantages over other methods of detecting chemical changes in-vivo. The first is that it is able to identify numerous neruochemcials in a single sample. In our study ten neurochemicals were chosen.

The other advantage of MRS is that it can potentially be performed non-invasively. A sample spectrum from an excised and processed rat spinal cord is shown in figure 4.7. The singlet resonance of DSS is used to define 0ppm and is not shown in this sample; the DSS peaks seen in this sample at 1.75 ppm and 2.9 ppm are from 2 as opposed to the nine protons of the reference singlet and are spread out over multiplets. A large lactate doublet can be seen at 1.3 ppm this was not measured because lactate rises considerably during the extraction process. The NAA and NAAG singlets just over 2 ppm are easily measured in-vitro but will likely prove difficult to separate in-vivo. We did measure several small multiplets between the NAA singlet at 2.0 ppm and the creatine singlet at 3.0 ppm, such as GABA at 2.29 ppm, glutamate at 2.35 ppm, glutamine at at 2.44 ppm. As can be seen in figures 4.10a, 4.10b and 4.11a the signal to noise ratio and spectral fit on these peaks is not nearly as nice as it is on the creatine and choline singlets in figure 4.9a and 4.9b. The choline, phosphorylcholine, and glycerophosphorylcholine around 3.2 ppm can be separated out in this sample but again would be difficult to separate in-vivo; even in this sample there is overlap between the phosphorlocholine and glycerophosphorylcholine

peaks. Both glycine's singlet at 3.55 ppm and the myo-inositol triplet at 3.61 ppm are easily distinguishable. The glycerol multiplet at 3.64, as shown in figure 4.10a, suffers both because it is a low intensity multiplet and is close enough to the myo-inositol triplet that further distorts its signal.

The mean ± SD control concentrations of all ten metabolites are shown in figure 4.8. The experimental in-vitro spectroscopic data are summarized in figures 4.9, 4.10, 4.11, 4.12 and 4.13. Figures 4.9a-4.13a, and 4.9b-4.13b contain the individual experimental spectral signals from each of the 10 measured metabolites (solid lines) together with the spectral fit used to quantify them (dashed line). The concentration normalized to the corresponding section of the control sample, are shown in figure 4.9c-4.13c and 4.9d-4.13d.

Comparison between the control concentration and each of the time points for a given location were made using an independent sample t-test $\alpha=0.05$. Comparisons were then made between the different segments of the cord at a given time point post-injury using an independent sample t-test $\alpha=0.05$.

The graphs in figure 4.9c-4.13c and 4.9d-4.13d indicate that the injury caused a statistically significant temporal change

mostly in non-neurotransmitter metabolites. Spacial changes were seen in all metabolites except choline, GABA, glycerol, and glycine. Most of the spatial changes were between the lesioned segment and its neighbors.

Choline showed significant differences at 1 day between rostral and lesioned segment and at 1 week between a reduced rostral and an increased caudal segment. Choline is used to make the neurotransmitter acetylcholine and a cellular membrane component phosphatidylcholine. The choline increase in the caudal section at one week is a potential sign of membrane breakdown.

Phosphocreatine is a cellular energy source; unfortunately only total creatine can be measured using proton spectroscopy. The total creatine concentration showed an increase at 1 week in the caudal segment with respect to the control. At 24 hours there was a decrease in the lesioned segment compared to the rostral segment and at one week after the injury the caudal segment increased significantly compared to the other two sections. These spatial differences may indicate the loss of spinal cord tissue and its replacement with glial scaring.

Glutamate, unlike previous studies [28,29] where its

increase was one method of excitotoxicity, did not show an immediate increase. To observe this spike it may require smaller sample sizes, 3mm, and shorter time periods, 2.5h, as used in previous studies. Glutamate did show an increase in the caudal segment at one week after injury both with respect to the control and the other 2 segments.

Myo-inositol is a marker for glial cells and its initial decline in the lesioned segment compared to the caudal and rostral segments from 4 hours after injury to 1 week followed by a increase in all three segments could indicate regrowth or remylination of axons by glial cells. The increase throughout the cord and the ability to measure myo-inositol in-vivo suggest that this could be a useful marker of recovery after spinal cord injury.

N-Acetyl Aspartate(NAA) concentrations in the lesioned segment dropped compared to the caudal sections within four hours after injury. Compared to the control concentration NAA in the lesioned segment was depressed at 24 hours and remained low for the next 4 weeks. This is consistent with previous studies [51] showing a decrease in NAA around spinal cord injury. This decrease may be a result of decreased neuronal function or even a decrease in neuronal density. This decrease is useful as NAA is

one of the most prominent peaks visible in in-vivo MRS.

N-Acetyl Aspartate Glutamate (NAAG) concentrations decreased significantly in the lesioned segment at 24 hour after the injury and remained low at 4 weeks after the injury. The spatial comparison showed NAAG in the lesioned segment dropping at one day after injury and remaining low. These changes are likely the result of dead and dying cells in the lesioned segment of the cord and given NAAG's neuroprotective effect this may exacerbate neuronal damage.

This study showed measurable changes in NAA a potential neuronal marker and a prominent in-vivo MRS peak and Myo-inositol, a glial cell marker that is also detectable in-vivo. Creatine changes indicative of glial scarring should also be detectable in-vivo.

An in-vivo scan was conducted on the spinal cord of a cat to explore the in-vivo potential of MRS, the resulting spectrum is shown in figure 4.14.

Transverse image of the lumbar spine

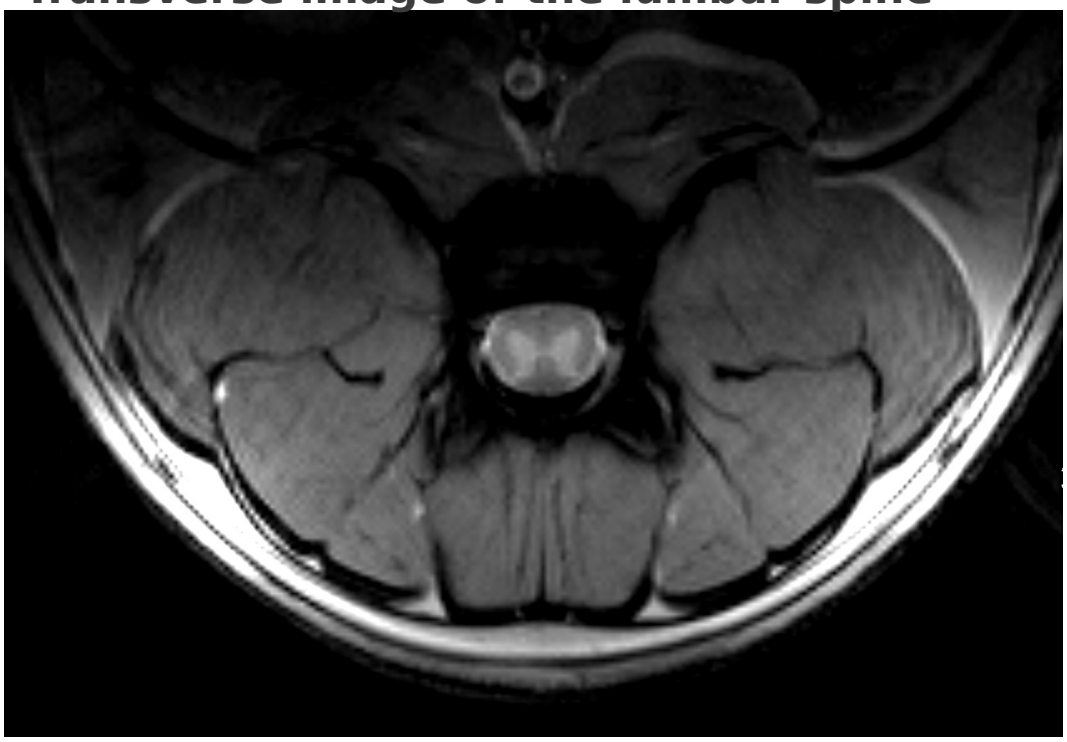

Transverse map of the lumbar spine

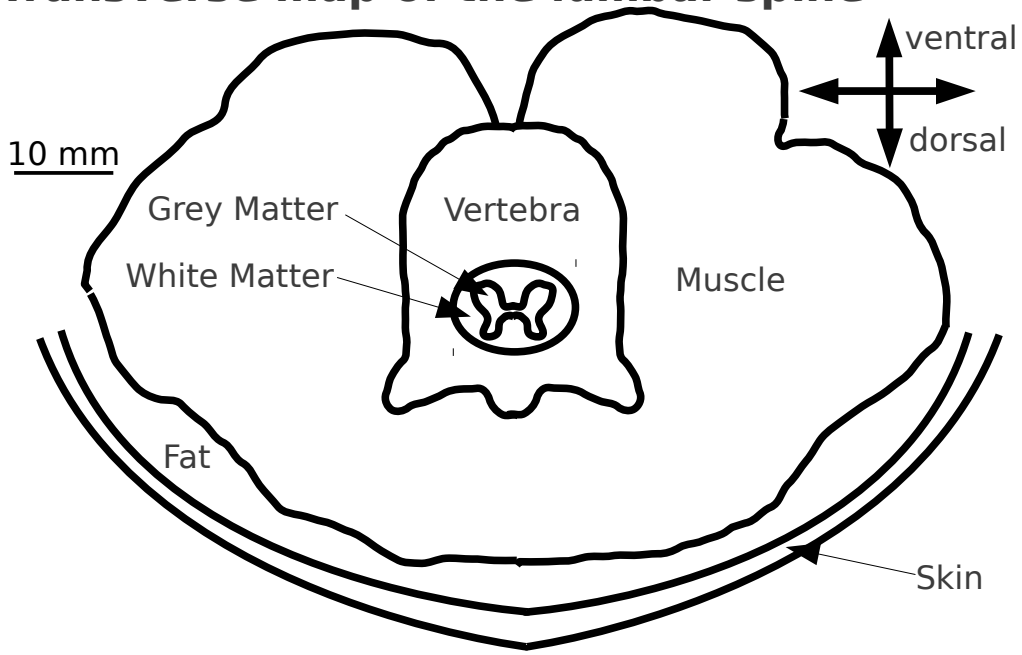

Figure 4.1 Transverse GE image of a cats lumbar spinal cord and a map for a transvese image of a cats lumbar spinal cord.

Coronal image of the lumbar spine

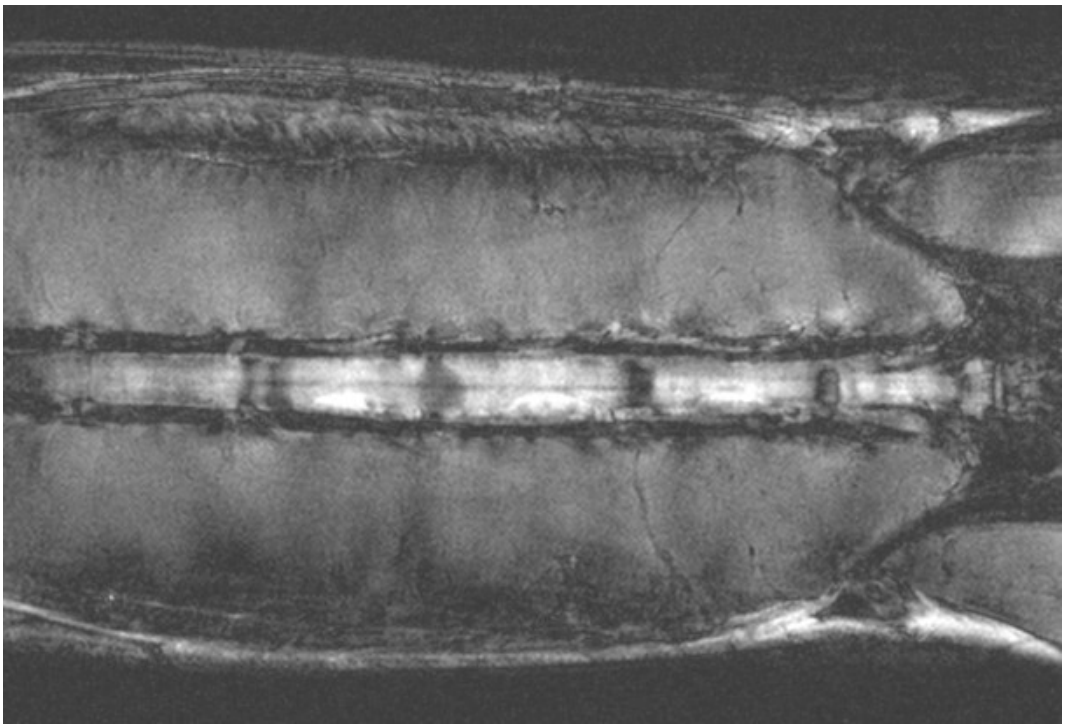

Coronal map of the lumbar spine

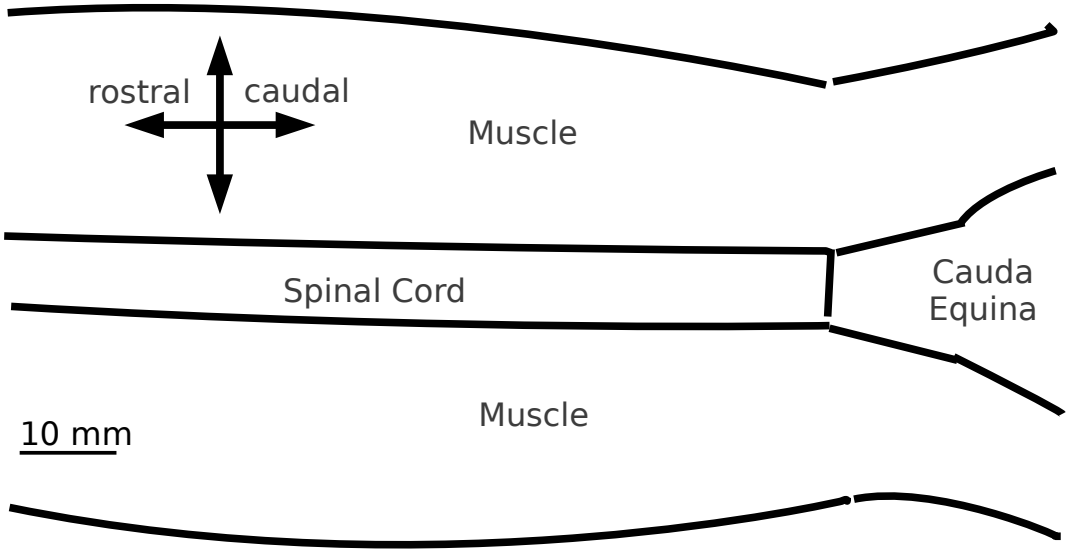

Figure 4.2 Coronal gradient echo image of a cats lumbar spinal cord and A map for a coronal image of a cats lumbar spinal cord.

Sagittal image of the lumbar spine

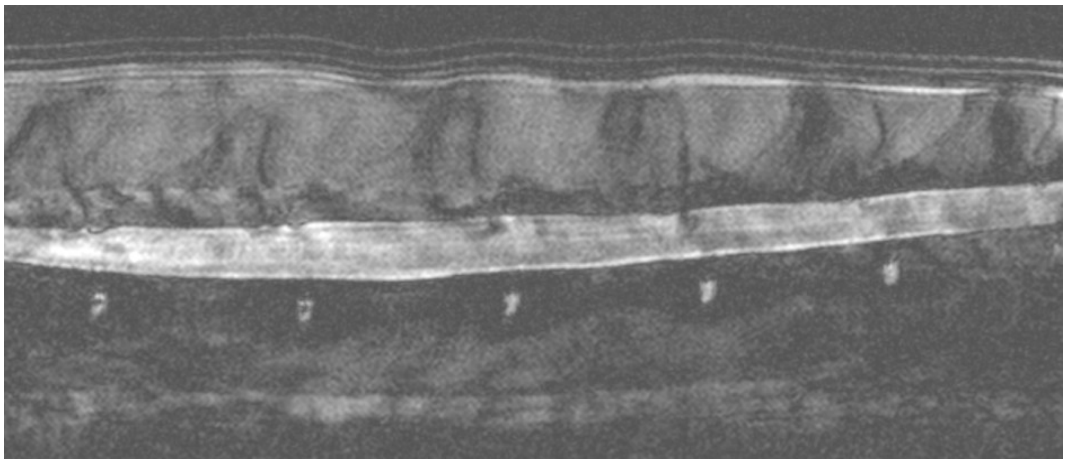

Sagittal map of the lumbar spine

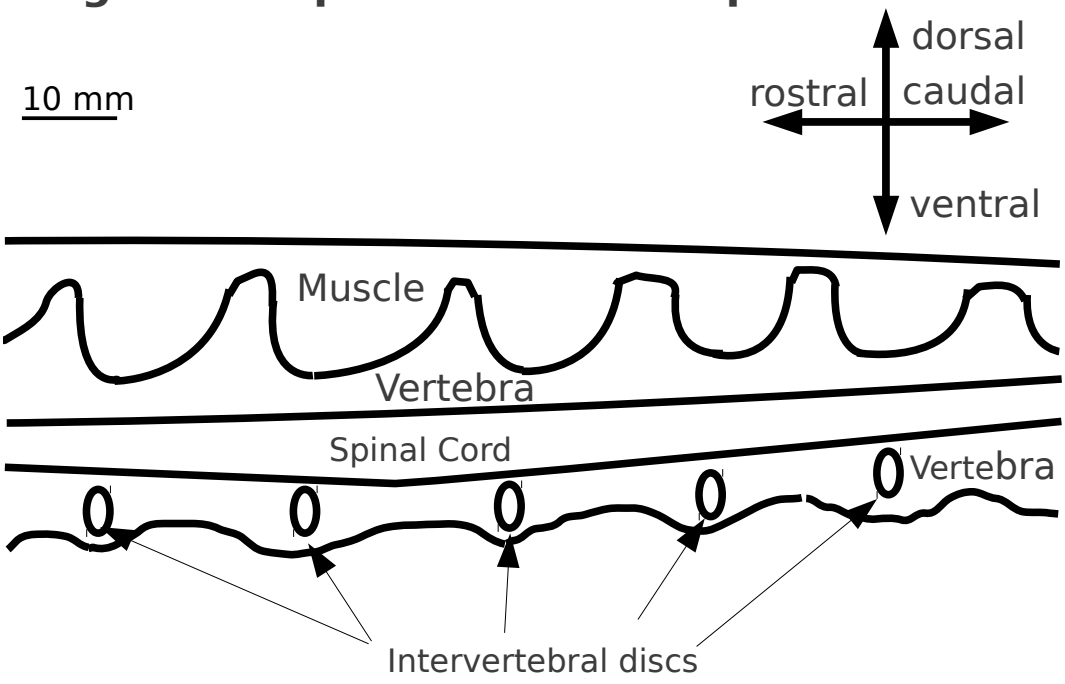

Figure 4.3 Sagittal gradient echo image of a cats lumbar Spinal cord and a map for a sagittal image of a cats lumbar spinal cord.

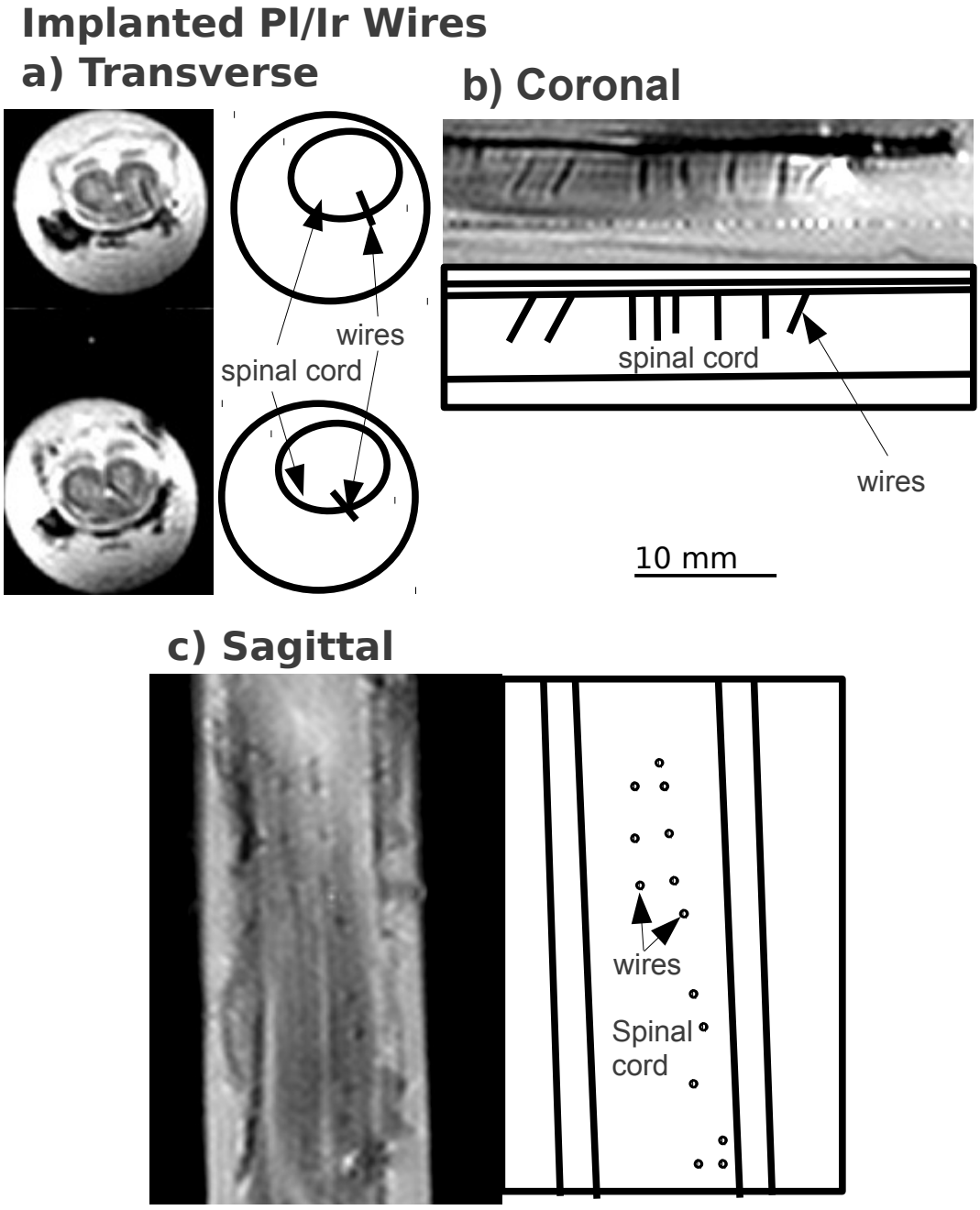

Figure 4.4 a) Two transverse spin echo images of a cats spinal cord implanted with micro-wires in a water filled test tube b) A coronal spin echo image of a cats spinal cord implanted with micro-wires in a water filled test tube. c) A sagittal spin echo image of a cats spinal cord implanted with micro-wires in a water filled test tube

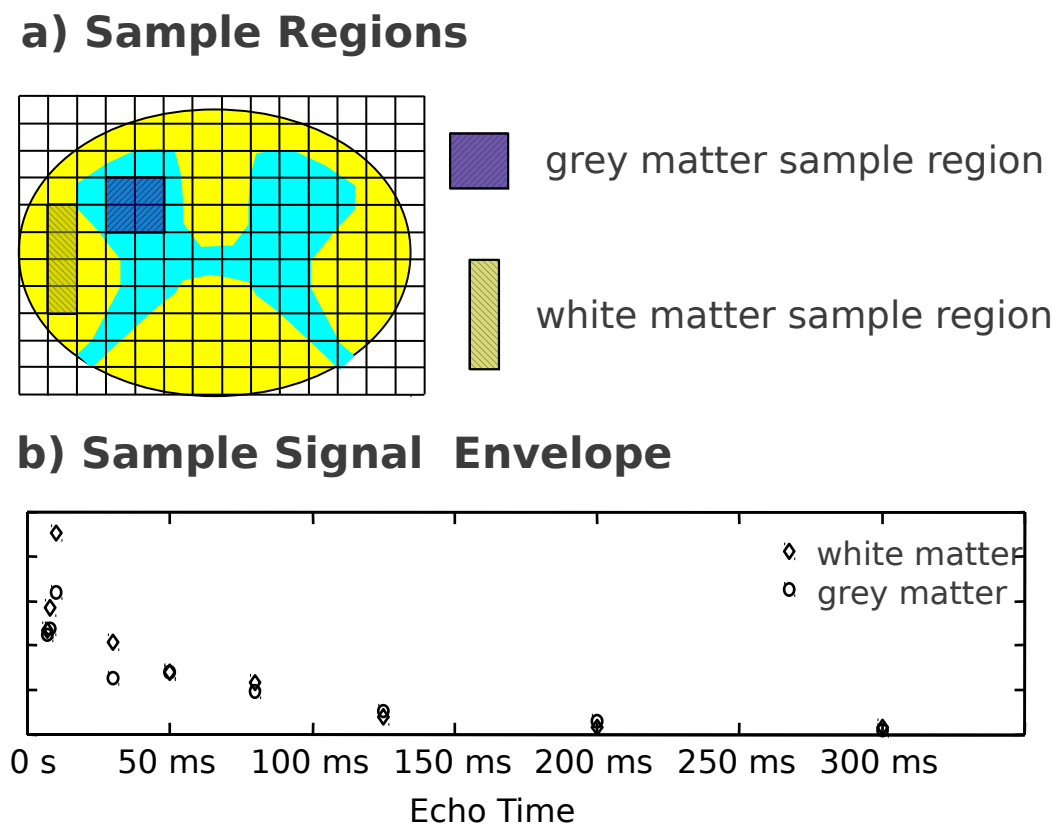

Figure 4.5 a) The sample regions in the feline spinal cord used to create the signal envelope. b) Sample intensity of values vs time for white and grey matter used to create an exponential signal envelope. c) Resulting T2 distribution from white and grey matter signal envelopes in figure 4.9b

T2 distributions

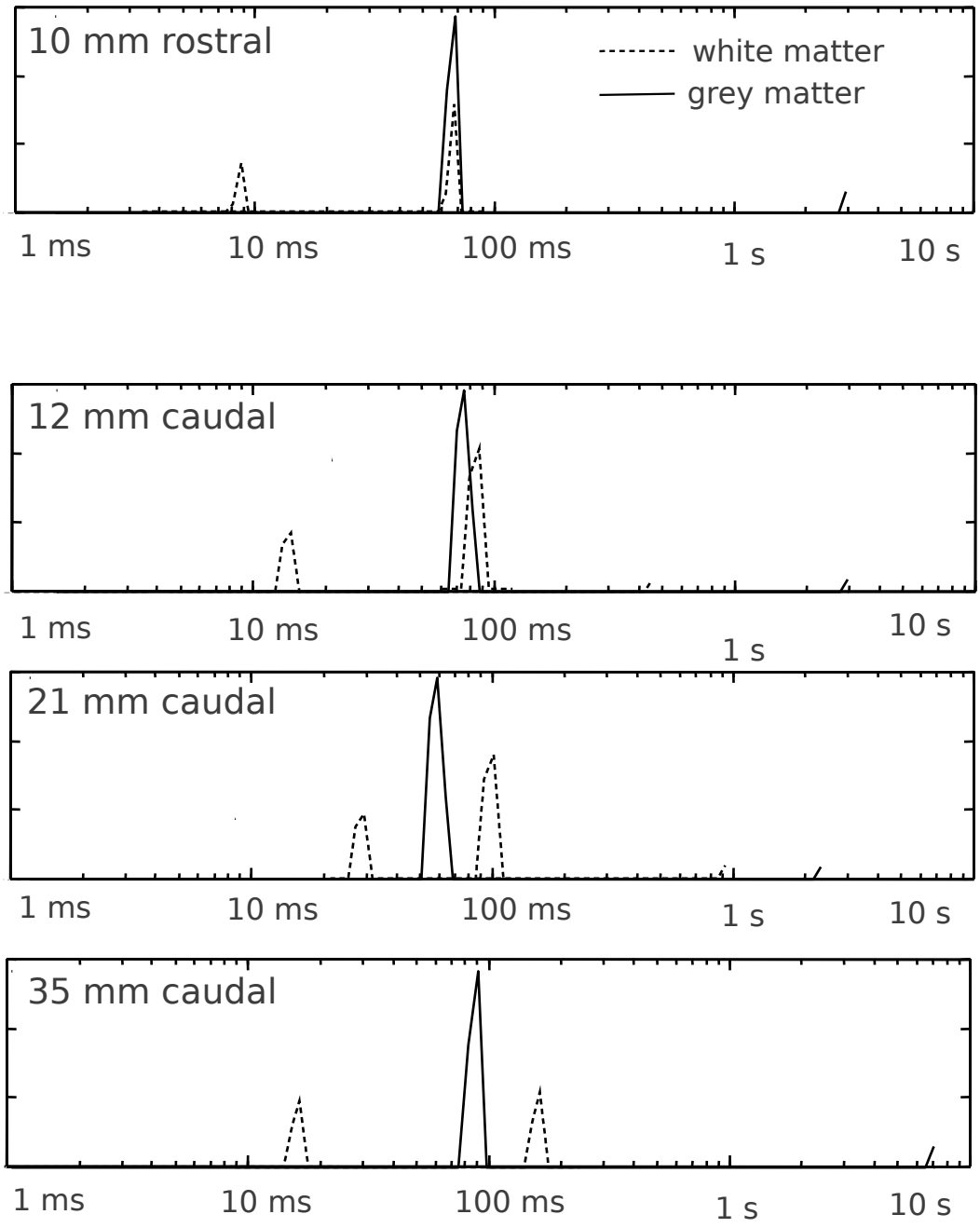

Figure 4.6 T2 distributions at from 10 mm rostral to 35 mm caudal from a lesion

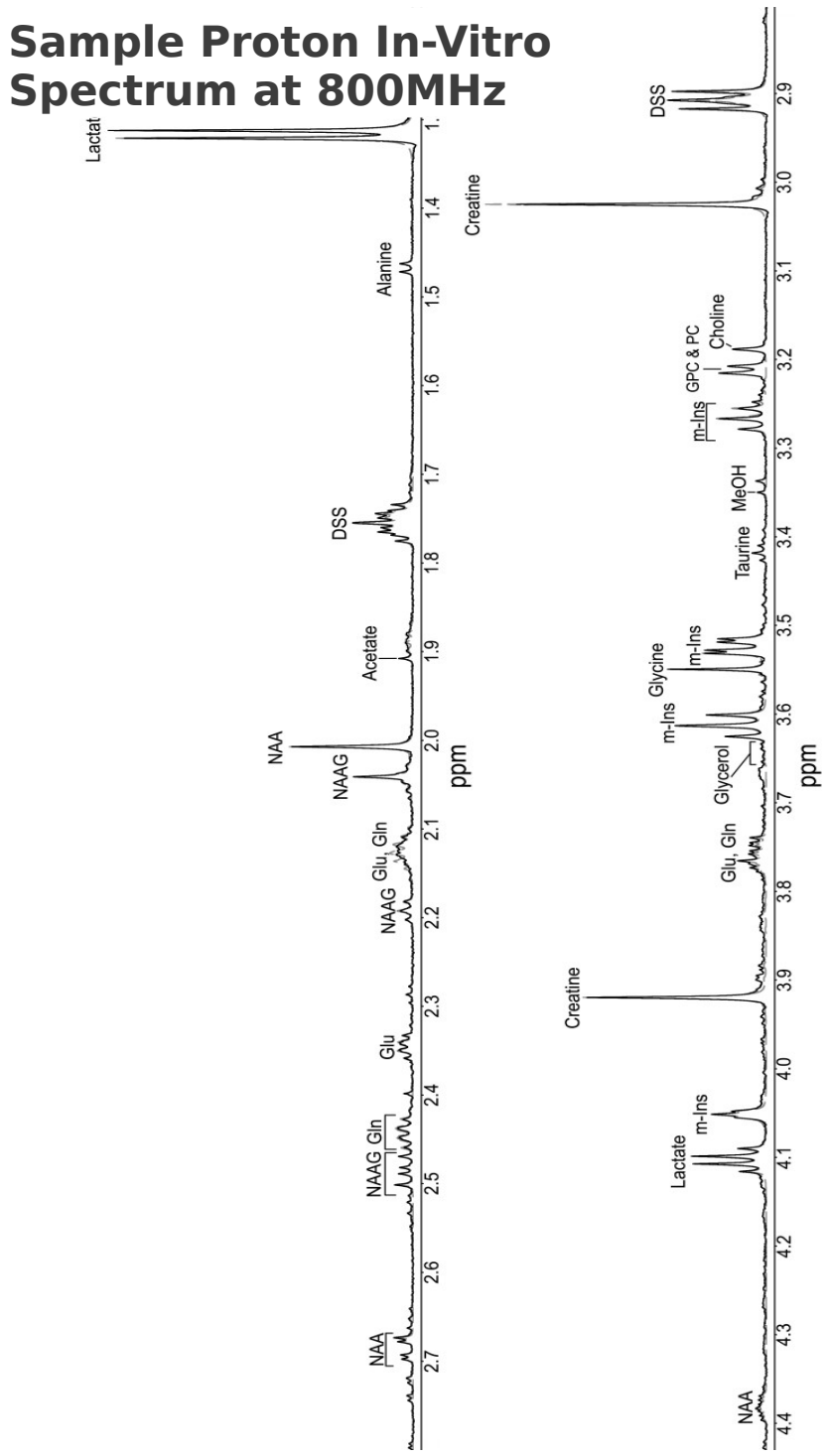

Figure 4.7 A sample proton in-vitro spectrum at 800 MHz from a rats spinal cord

Control Concentrations

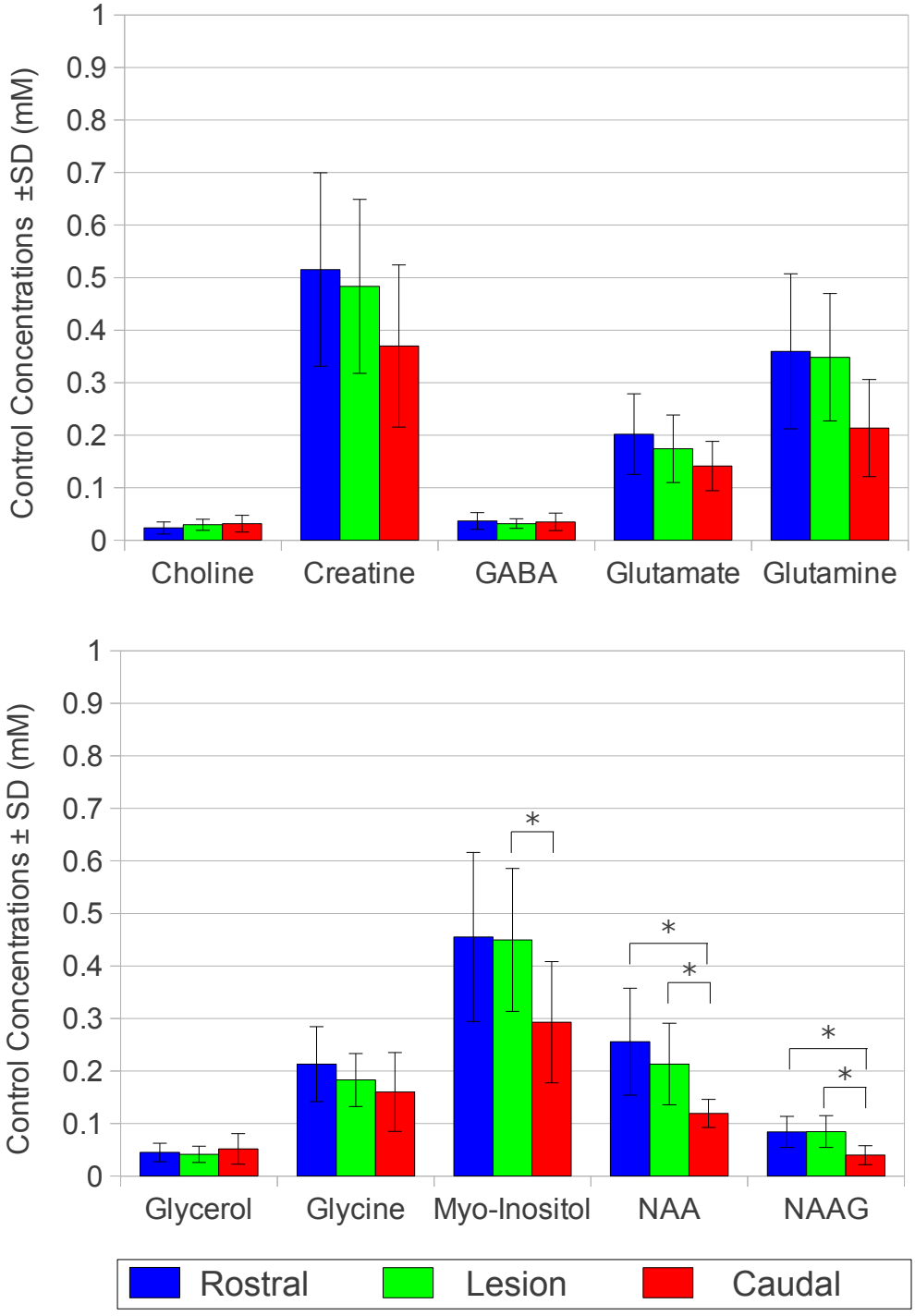

Figure 4.8 Average metabolite concentrations from the Control group ± standard deviations. Significant differences ($p \leq 0.05$) are indicated with *.

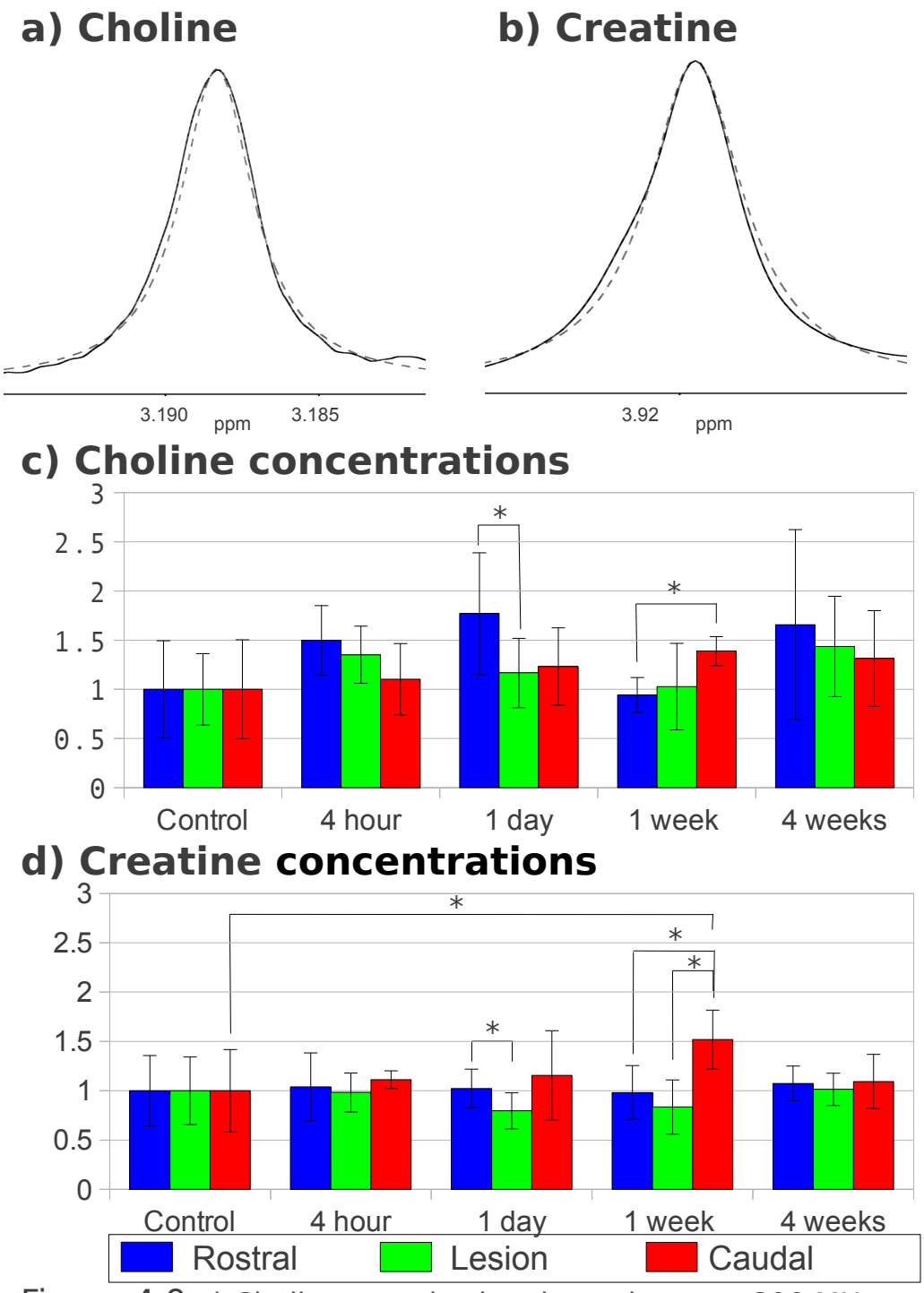

Figure 4.9 a) Choline sample signal envelopes at 800 MHz. b) Creatine sample signal envelope at 800 MHz. c) Choline concentrations normalized to control ± standard deviation. d) Creatine concentrations normalized to control ± standard deviation. * denotes statistical significance

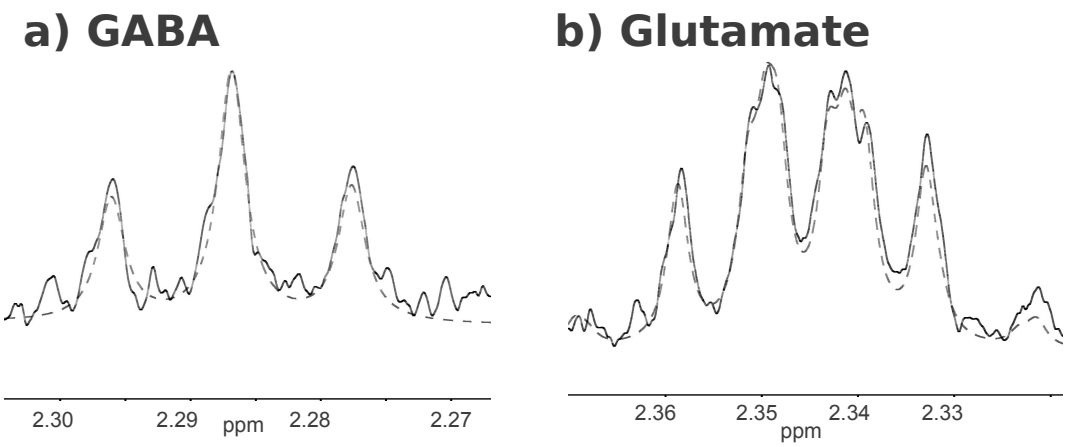

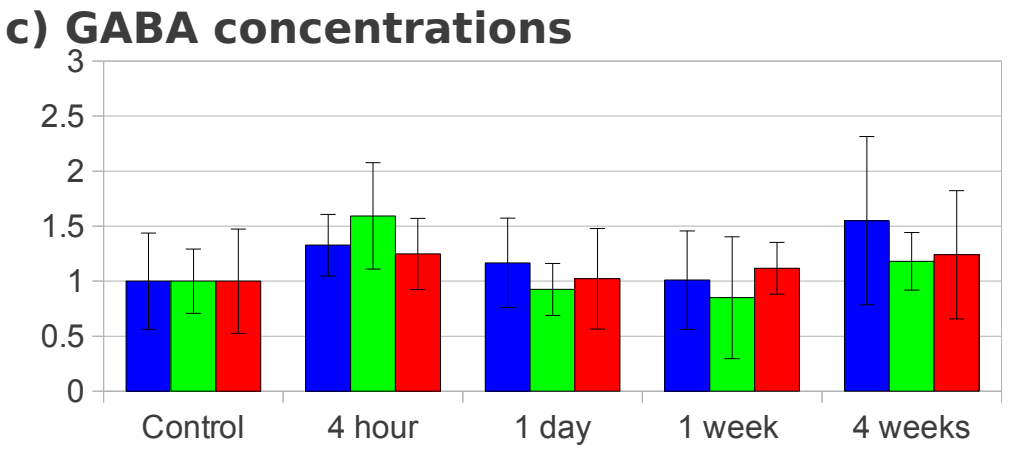

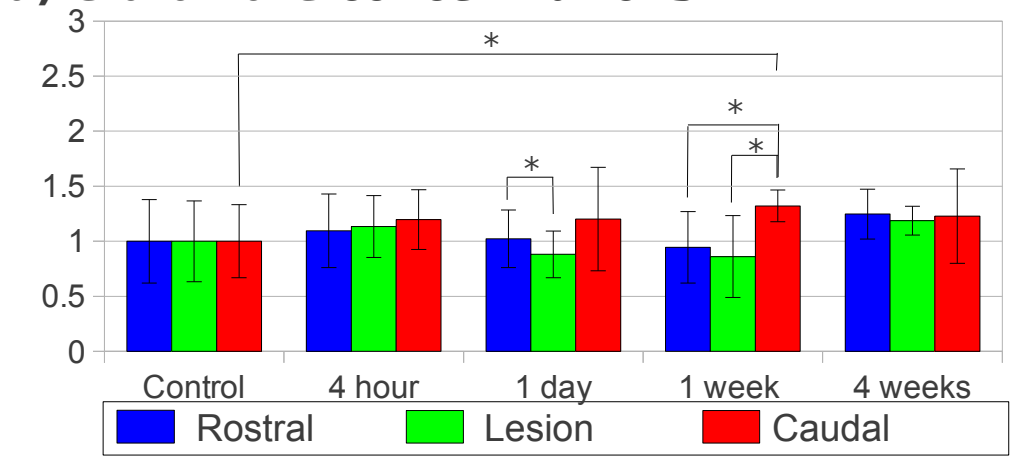

Figure 4.10 a) GABA sample signal envelope at 800 MHz. b) Glutamate sample signal envelope at 800 MHz. c) GABA concentrations normalized to control ± standard deviation. d) Glutamate concentrations normalized to control ± standard deviation. * denotes statistical significance

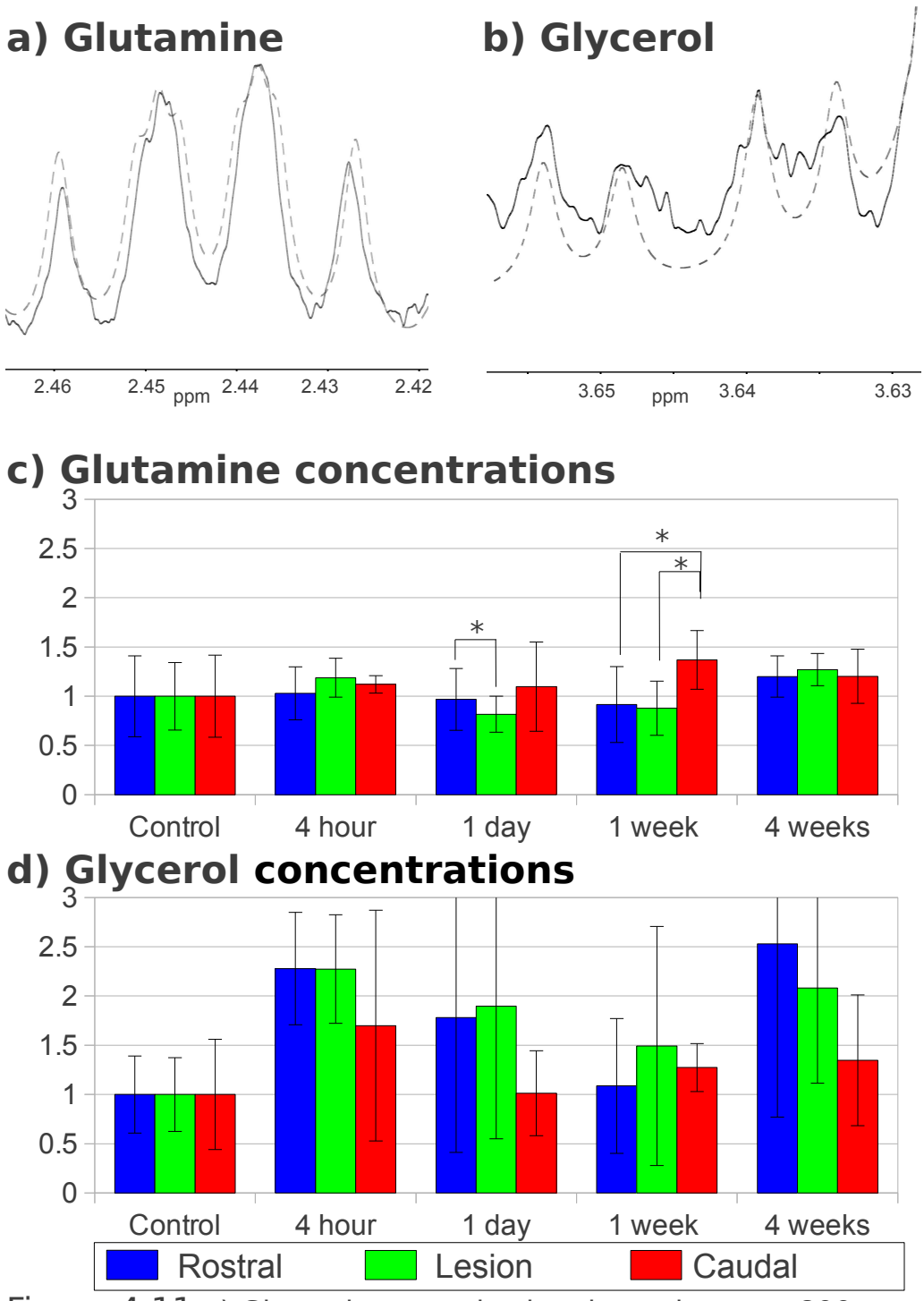

Figure 4.11 a) Glutamine sample signal envelopes at 800 MHz. b) Glycerol sample signal envelope at 800 MHz. c) Glutamine concentrations normalized to control ± standard deviation. d) Glycerol concentrations normalized to control ± standard deviation. * denotes statistical significance

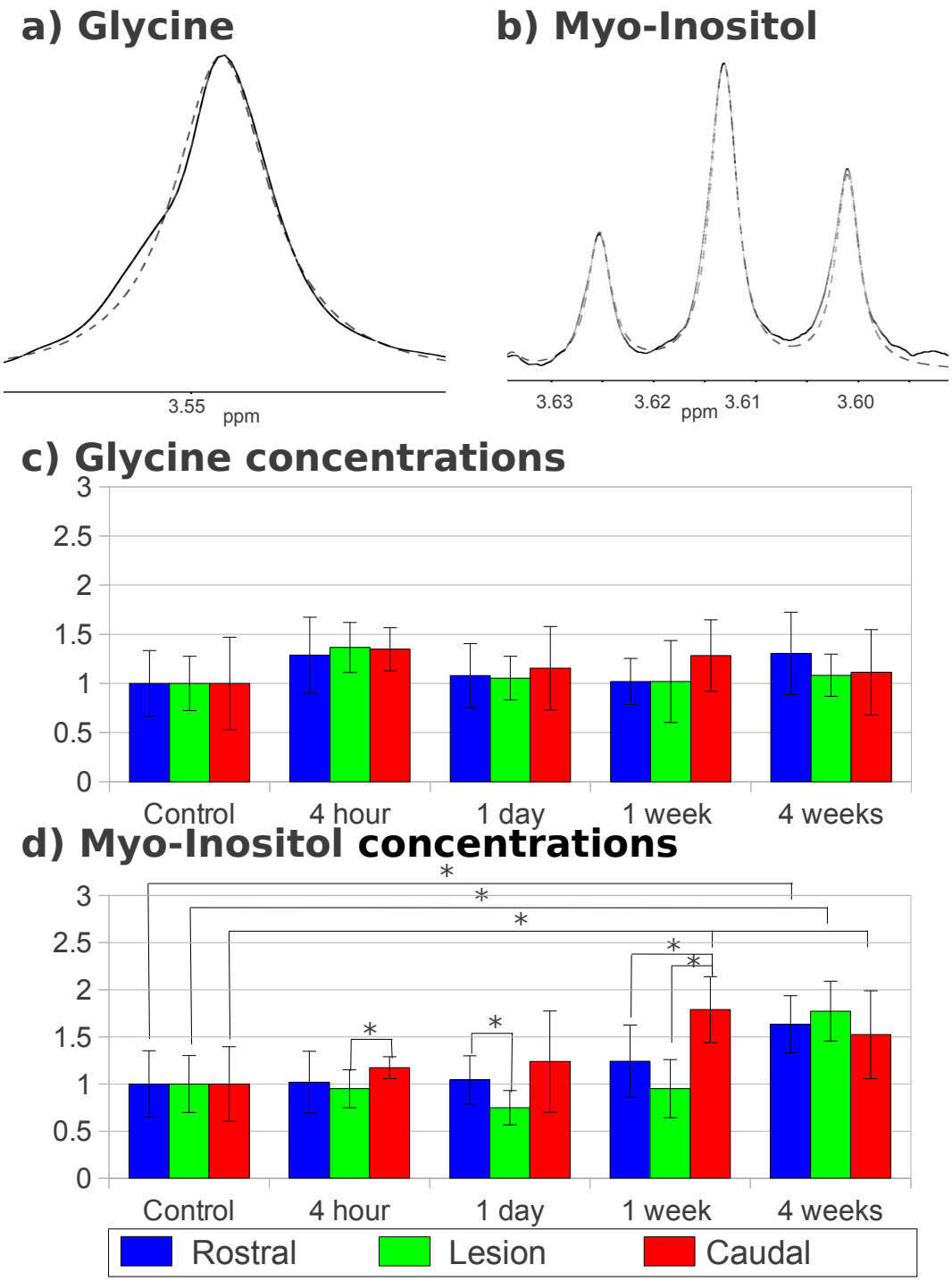

Figure 4.12 a) Glycine sample signal envelopes at 800 MHz. b) Myo-Inositol sample signal envelope at 800 MHz. c) Glycine concentrations normalized to control ± standard deviation. d) Myo-Inositol concentrations normalized to control ± standard deviation. * denotes statistical significance

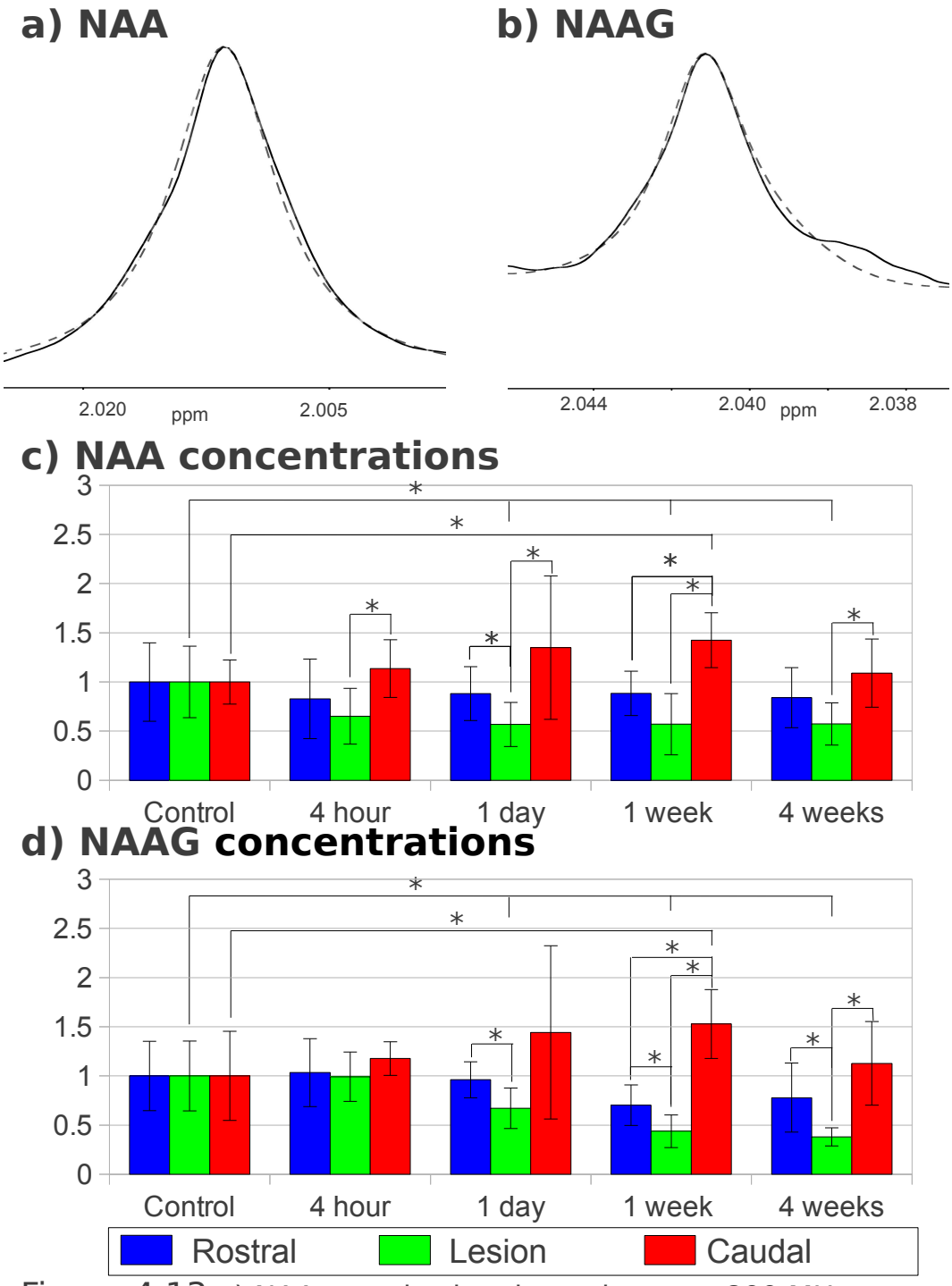

Figure 4.13 a) NAA sample signal envelopes at 800 MHz. b) NAAG sample signal envelope at 800 MHz. c) NAA concentrations normalized to control ± standard deviation. d) NAAG concentrations normalized to control ± standard deviation. * denotes statistical significance

In vivo Spectrum at 127 MHz

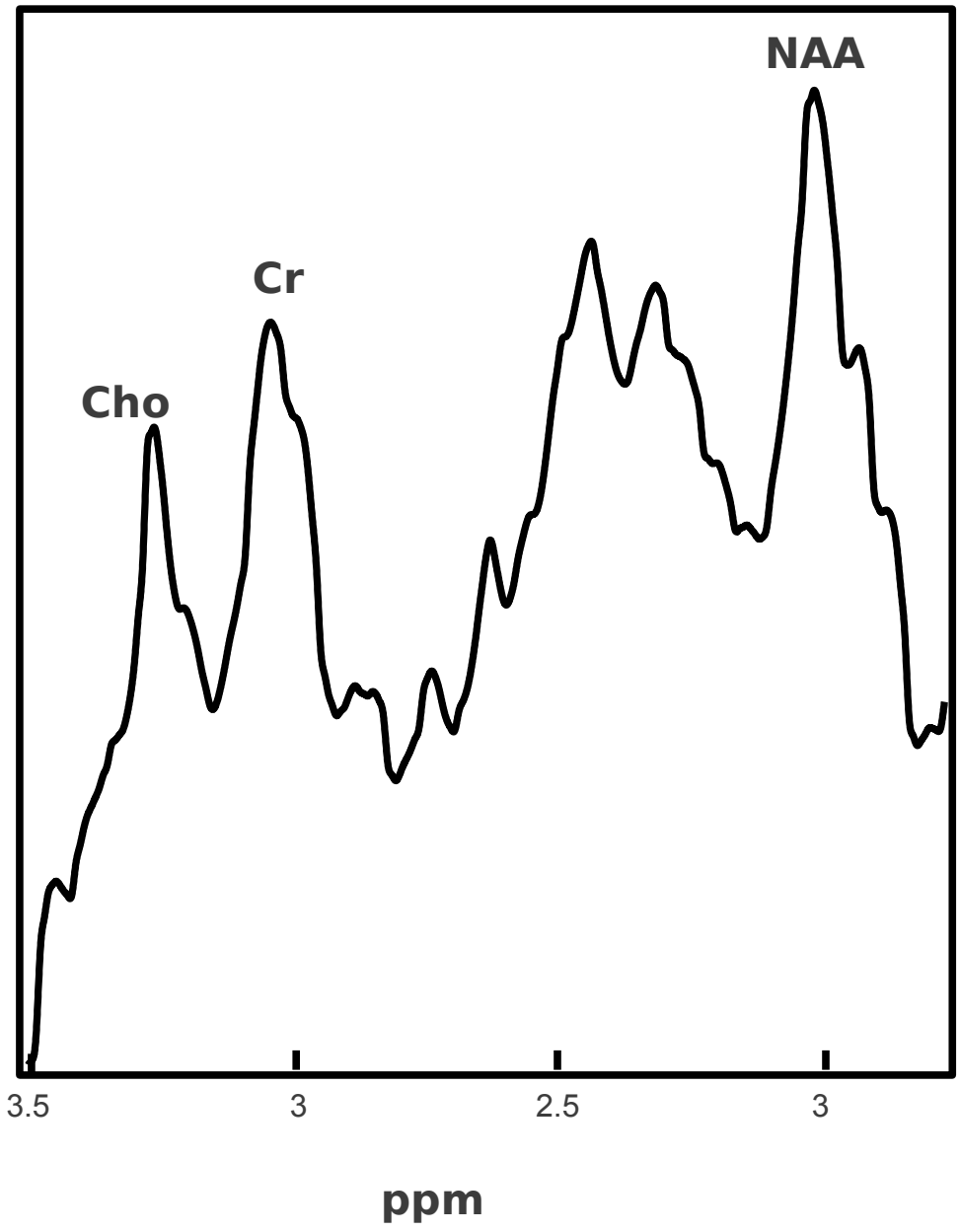

Figure 4.14 A sample in vivo spectrum at 127 MHz from a cats lumbar spinal Cord, identifying choline, creatine, and NAA peaks.

5. Conclusions

The rationale of this Masters program was to explore the potential of MR as an investigative tool in the analysis of spinal cord injury and the effects of potential treatments. The ultimate goal would be to use MR as a non-invasive method to both analyzed the cellular and chemical ramifications of spinal cord injury and to assist in the development of novel treatments of spinal cord injury. In doing this, three capabilities of MR were evaluated, namely, the imaging of the spinal cord and metallic implants along with their surrounding tissue, see section 5.1; the compartmentalization of water within biological structures, see section 5.2; and the ability of MR to monitor the different spectroscopic signatures of certain metabolites, see section 5.3.

5.1 Imaging

The work reported in this study showed that with specialized radio frequency coils it is possible to obtain images of the spinal cord in a feline model with good grey matter/white matter contrast and resolution. It was also demonstrated that

MRI can be used to locate precisely the micro-wires that are used for ISMS; this initial demonstration being carried out on excised spinal cords. Imaging micro-wires in-vivo would be the next step for this study to take. Beyond that, building larger coils, and imaging the human spinal cord, as was done on feline models, would be a future objective. Although in this study I did not have the opportunity of imaging various types of spinal cord injuries in detail, more recent work [52] has looked at MRI of spinal cord injuries, and correlat, MRI with clinical impairment scales[53]. Other MRI techniques such as diffusion tensor imaging and magnetization transfer[54,55,56,57] have also shown promise in assessing spinal cord injury. As higher field imaging magnets have become available imaging of spinal cord injury has also been done at 7T[58].

5.2 Water Compartmentalization

Using custom coils this thesis demonstrated that two of the four components identified by previous in-vitro studies of central nervous system tissue can be resolved in-vivo. The first of these components is from myelin water and is only found in white

matter. The second component found in both gray and white matter is attributed to axonal and extracellular water. Two very small components seen in extract studies were not observed in-vivo.

Further studies [59,60] have been able to resolve these components in adult humans and have seen changes in myelin water fraction with respect to age. Other studies have focused on optimizing echo spacing in CPMG sequences to better measure water components[61]. Comparison of histology and T_2 distributions has also been performed[62]. Yet to be done would be determining if changes in the component ratios or times vary with time after injury.

5.3 In-Vitro MR Spectroscopy

In-vitro MRS was shown to be capable of identifying the long term changes in certain metabolites following injury, namely, an increase in myo-inositol, and a decrease in the neuroprotective NAAG. NAA decreased with time following injury and considering that NAA is one of the easier signals to detect in-vivo is promising. The molecular structure of some metabolites are so similar that even in-vitro at 800 MHz it was not possible to

distinguish them from one another. Such an example was the group of free choline, glycerophosphorylcholine, and phosphorylcholine. A similar indistinguishable pair is creatine and phosphocreatine. Though these metabolites are indistinguishable in proton NMR phosphorus NMR could be used to differentiate them.

Although no extensive in-vivo spectroscopy work was completed, a proof of concept scan showed that it is possible to resolve relative levels for at least creatine, choline, and NAA concentrations. Other studies have since looked at measuring glutamate, creatine, NAA, choline, and myo-Inositol in the spinal cord in-vivo [60,63,64,65,66].

5.4 Clinical Applications

Imaging of the spinal cord and of spinal cord injuries are the portions of this thesis that can be most readily implemented clinically. The imaging of the spinal cord as done in this thesis is the basis of imaging spinal cord injuries. These images are important not only to assess the severity of a spinal cord injury but also to assist in treatments ranging from surgery to remove damaged tissue to implantation of devices such as the micro-

wires used in ISMS.

The clinical advantages of water compartmentalization are not as clear but with its ability to look at both myelin water fraction and potentially the freedom of water movement it may be possible to use T_2 distributions to evaluate inflammation.

As the ability to perform more detailed spectroscopy in vivo advances the measurement of metabolites such as glutamate, NAAG, and myo-Inositol in vivo in the spinal cord becomes possible. This study identified several metabolites that change with respect to time and position of the injury. Knowing these trends and the current level of metabolites in the spinal cord would allow not only the selection of appropriate drug treatments but for the customization of those treatments for a specific patient before functional outcomes are observable.

5.5 Summary

Nuclear magnetic resonance techniques show some significant promise in imaging the spinal cord, assessing the spinal cord with water compartmentalization or magnetic resonance spectroscopy, and assisting in novel treatments such as ISMS.

Bibliography

Overview

[1] Srivastava R, Murphy MJ, Jeffery J. Cerebrospinal Fluid : The Role of Biochemical Analysis, Br J Hosp Med 2008; 69:218-22.

[2] Seehusen DA, Reeves MM, Fomin DA. Cerebrospinal Fluid Analysis, Am Fam Physician 2003; 68:1103-1108.

[3] http://www.icord.org/

[4] http://www.canparaplegic.org/en/

[5] http://www.sci-info-pages.com/facts.html

[6] Schwab M, Bartholdi D. Degeneration and Regeneration of Axons in the Lesioned Spinal Cord. Physiol Rev 1996; 76:319-370

[7] Heindel W, Kugel H, Roth B. Noninvasive Detection of Increased Glycine Content by Proton MR Spectroscopy in the Brains of Two Infants with Nonketotic Hyperglycinemia. AJNR Am J Neuroradiol 1993; 14:629–635.

[8] Liu D, Xi G, Pan E, McAdoo D. Neurotoxicity of Glutamate at the Concentration Released Upon Spinal Cord Injury. Neuroscience 1999; 93:1383-1389

[9] Sibson N, Dhankar A, Mason G, Rothman D, Behar K, Shulman R. Stoichiometric Coupling of Brain Glucose Metabolism and Glutamatergic Neuronal Activity. Proc Natl Acad Sci USA 1998; 95: 316-321.

[10] Ross B. Biochemical Considerations in 1H Spectroscopy. Glutamate and Glutamine; myo- Inositol and Related Metabolites. NMR Biomed 1991; 4:59-63.

[11] Diaz-Ruiz A, Salgado-Ceballos H, Montes S, Maldonado V, Tristan L, Alcaraz- Zubeldia M, Ríos C. Acute Alterations of

Glutamate, Glutamine, GABA, and Other Amino Acids After Spinal Cord Contusion in Rats. Neurochem Res 2007; 32:57-63.

[11] Garnett M, Blamire A, Corkill R, Cadoux-Hudson T, Rajagopalan B, Styles P. Early Proton Magnetic Resonance Spectroscopy in Normal-Appearing Brain Correlates with Outcome in Patients Following Traumatic Brain Injury. Brain 2000; 123:2046-2054.

[12] Anderson D, Means E, Waters T, Spears C. Spinal Cord Energy Metabolism Following Compression Trauma to the Feline Spinal Cord. J Neurosurg 1980; 53:375-380.

[13] Saunders D, Howe F, van der Boogaart A, Griffiths J, Brown M. Aging of the Adult Human Brain: In Vivo Quantification of Metabolite Content with Proton Magnetic Resonance Spectroscopy. J Magn Reson Imaging 1999; 9:711-716.

[14] Moore G, Galloway M. Magnetic Resonance Spectroscopy: Neurochemistry and Treatment Effects in Affective Disorders. Psychopharmacol Bull 2002; 36:5-23.

[15] Coyle J. The Nagging Question of the Function of N-acetylaspartylglutamate. Neurobiol Dis 1997; 4:231-238.

[16]Lu X, Tang Z, Liu W, Lin Q, Slusher B. N-acetylaspartylglutamate Protects Against Transient Focal Cerebral Ischemia in Rats. Eur J Pharmacol 2000; 408:233-239.

Spinal cord injury basics

[17] Allen AR. Remarks on the Histopathological Changes in the Spinal Cord Due to Impact. An Experimental Study. J Am Med Ass 1911; 57:878-880

[18] Mautes AEM, Weinzierl MR, Donovan F, Noble LJ. Vascular Events After Spinal Cord Injury: Contribution to Secondary Pathogenesis. Phys Ther 2000; 80:673-678

[19] Zhang Z, Krebs CJ, Guth L. Experimental Analysis of

Progressive Necrosis after Spinal Cord Trauma in the Rat: Etiological Role of The Inflammatory Response. Exp Neurol 1997; 143:141-152.

[20] Martinez-Arizala A, Green BA. Hypothermia in Spinal Cord Injury. J Neruotrama 1992; 2:S497-505

[21] Means ED, Anderson DK, Waters TR, Kalaf L. Effect of Methylprednisolone in Compression Trauma of the Feline Spinal Cord. J Neurosurg 1981; 55:200-208

[22] Sandler AN, Tator CH. Review of the Effects of Spinal Cord Trauma on the Vessels and Blood Flow in the Spinal Cord. J Neurosurg 1976; 45:638-646

[23] Tator CH, Koyanagi I. Vascular Mechanisms in the Pathophysiology of Human Spinal Cord Injury. J of Neurosurg 1997; 86:483-492.

[24] Yourick DL, Koenig ML, Durden AV, Long JB. N-acetylaspartylglutamate and Beta-NAAG Protect Against Injury Induced by NMDA and Hypoxia in Primary Spinal Cord Cultures. Brain Res 2003; 991:56-64.

[25] Fawcett JW, Asher RA. The Glial Scar and Central Nervous System Repair. Brain Res Bull 1999; 49:377-391.

[26] Liu D, Liu J, Sun D, Alcock NW, Wen J; Spinal Cord Injury Increases Iron Levels: Catalytic Production of Hydroxyl Radicals. Free Radic Bio Med 2003; 34:64-71.

[27] http://www.exrx.net/Nutrition/Antioxidants/Introduction.html

[28] Xu GY, Hughes MG, Ye Z, Hulsebosch CE, McAdoo DJ. Concentrations of Glutamate Released Following Spinal Cord Injury Kill Oligodendrocytes in the Spinal Cord. Exp Neurol 2004; 187:329–336.

[29] Lepore AC, O'donnell J, Kim AS, Yang EJ, Tuteja A, Haidet-Phillips A, O'Banion CP, Maragakis NJ. Reduction in Expression of the Astocyte Glutamate Transporter, GLT1, Worsens Functional and Histological Outcomes Following

Tramatic Spinal Cord Injury. GLIA 2011; 59:1996-2005.

[30] Liu S, Ruenes GL, Yezierski RP. NMDA and non-NMDA Receptor Antagonists Protect Against Excitotoxic Injury in the Rat Spinal Cord. Brain Res 1997; 756:160-167.

[31] McAdoo DJ, Xu GY, Robak G, Hughes MG. Changes in Amino Acid Concentrations Over Time and Space Around an Impact Injury and Their Diffusion Through the Rat Spinal Cord. Exp Neurol 1999; 15:538-544.

[32] Diaz-Ruiz A, Salgado-Ceballos H, Montes S, Maldonado V, Tristan L, Alcaraz-Zubeldia M, Rios C. Acute Alterations of Glutamate, Glutamine, GABA, and Other Amino Acids After Spinal Cord Contusion in Rats. Neurochem Res 2007; 32:57-63.

[33] Markandaya M, Stein D, Acute Treatment Options for Spinal Cord Injury. Current Treatment Options in Neurology 2012; 14:175-187.

[34] Kralj A, Acimovic R, Stanic U. Enhancement of hemiplegic patient rehabilitation by means of functional electrical stimulation. Prosthetics and Orthotics International 1993; 17:107-114.

[35] Prochazka A, Mushahwar VK. Spinal cord function and Rehabilitation and Overview. J of Physiology 2001; 533:3-4.

[36] David S, Zarruk JG, Ghasemlou N. Inflammatory Pathways in Spinal Cord Injury. Int Rev Neurobiol 2012; 106:127-152

NMR basics

[37] Hahn EL. Spin Echoes. Phys Rev 1950; 50:580-601.

[38] Carr HY, Purcell EM. Effects of Diffusion in Nuclear Magnetic Resonance Experiments. Phys Rev 1954; 94:630-638.

[39] Govindaraju V, Young K, Maudsley AA. Proton NMR Chemical Shifts and Coupling Consants for Brain Metabolites. NMR in

Biomed 2000; 13:129-153.

Methodology

[40] Lauterbur PC. Image Formation by Induced Local Interactions: Examples Employing Nuclear Magnetic Resonance. Nature 1973; 242:190-191.

[41] Melboom S, Gill D. Modified Spin-Echo Method for Measuring Nuclear Relaxation Times. Rev Sci Instrum 1958; 29:688-691.

[42] Lawson CL, Hanson BJ. (1974), Solving Least Squares Problems, Prentice-Hall (Englewood Cliffs, NJ).

[43] O'Donnell T, Rotzinger S, Nakashima TT, Hanstock CC, Ulrich M, Silverstone PH. Chronic Lithium and Sodium Valproate Both Decrease the Concentration of Myoinositol and Increase the Concentration of Inositol Monophosphates in Rat Brain. Eur Neuropsychopharmacol. 2003;13:199-207.

[44] Bligh EG, Dyer WJ. A Rapid Method of Total Lipid Extraction and Purification. Can J Biochem Physiol. 1959; 37:911-917.

[45] Edhwrudjakpor PO, Miyake H, Kurisaka M, Mori K. Central Nervous System Bioaminergic Responses to Mechanical Trauma. Surg Neurol. 1991; 35:273-279.

Results

[46] Ernst RR, Anderson WA. Applications of Fourier Transform Spectroscopy to Magnetic Resonance 1966; 37:93-102

[47] Bjarnason TA, Vavasour IM, Chia CL, MacKay AL. Characterization of the NMR Behavior of White Matter in Bovine Brain. Magn Reson Med 2005; 54:1072-1081

[48] Menon RS, Allen PS. Application of Continuous Relaxation

Time Distribution to the Fitting of Data from Model Systems and Excisied Tissue. Magn Reson Med 1991; 20:214-227

[49] De Stefano N, Matthews PM, Arnold DL. Reversible Decreases in N-acetylaspartate After Acute Brain Injury. Magn Reson Med 1995; 34:721-727.

[50] Graham LT, Shank RP, Werman R, Aprison MH. Distribution of Some Synaptic Transmitter Suspects in Cat Spinal Cord: Glutamic Acid, Aspartic Acid, Gamma-aminobutyric Acid, Glycine and Glutamine. J Neurochem 1967; 14:465-472.

[51] Falconer JC, Liu SJ, Abbe RA, Narayana PA. Time Dependence of N-acetyl-aspartate, Lactate, and Pyruvate Concentrations Following Spinal Cord Injury. J Neurochem 1996; 66:717-72.

Conclusions

[52] Karpova A, Arun R, Cadotte DW, Davis AM, Kulkarni AV, O'Higgins M, Fehlings MG. Assesment of Spinal Cord Compression by Magnetic Resonance Imaging -Can it Predict Surgical Outcomes in Degenerative Compression Myelopathy?: A Systematic Review. Spine 2013; 000:000-000.

[53] Parashari UC, Khanduri S, Bhadury S, Kohli N, Parihar A, Singh R, Srivastava RN, Upadhyay D. Diagnostic and Prognostic Role of MRI in Spinal Trauma, its Comparison and Correlation with Clinical Profile and Neurological Outcome, According to ASIA Imparment scale. J Craniovertebr Junction Spine. 2011; 2:17-26

[54] Bazley FA, Pourmorteza A, Gupta S, Pashai N, Kerr C, ALL AH. DTI for Assessing Axonal Integrity After Contusive Spinal Cord Injury and Transplantation of Oligodendrocyte progenitor cells. Conference Procedings IEEE Eng, Med Biol Soc. 2012:82-85.

[55] Rajasekaran S, Kanna RM, Shetty AP, Ilayaraja V. Effeciancy of Diffusion Tensor Anisotropy Indices and Tractography in

Assessing the Extent of Severity of Spinal Cord Injury: An In vitro Analytical Study in Calf Spinal Cords. Spine J 2012; 12:1147-1153.

[56] Smith SA, Pekar JJ, Van Ziji PC. Advanced MRI Strategies for Assessing Spinal Cord Injury. Handb Clin Neurol 2012; 109:85-101.

[57] Wang W, Qin W, Hao N, Wang y, Zong G. Diffusion Tensor Imaging in Spinal Cord Compression. Acta Radiol. 2012; 53:921:928.

[58] Cohen-Adad J, Zhao W, Wald LL, Oaklander AL. 7T MRI of Spinal Cord Injury. Neurobiology 2012; 79:2217.

[59] MacMillan EL, Madler B, Fichtner N, Dvorak MF, Li DKB, Curt A, Mackay AL. Myelin Water and T2 Relaxation Measurements in the Healthy Cervical Spinal Cord at 3T: Repeatability and Changes With Age. Neuroimage 2011; 54:1083-1090.

[60] Meyers SM, Vavasour IM, Madler B, Harris T, Fu E, Li DK, Traboulsee AL, Mackay AL, Lauie C. Multicenter Measurements of Myeline Water Fraction and Geometric Mean T2: Intra-and inter-site Reproducibility. J Magnetic Resonance Imaging 2013; 000:000-000

[61] Dula AN, Gochberg DF, Does MD. Optimal Echo Spacing for Multi-Echo Imaging Measurements of Bi-Exponential T2 Relaxation. J Magnetic Resonance 2009; 196:149-56

[62] Dula AN, Gochberg DF, Valentine HL, Valentine WM, Does MD. Multiexponential T2 Magnetization Transfer, and Quantitative Histology in White Matter Tracts of the Rat Spinal Cord. Magnetic Resonance in Medicine 2010; 63: 902-909

[63] Qian J, Herrera J, Narayana P. Neuronal and Axonal Degeneration in Experimental Spinal Cord Injury: in Vivo Proton Magnetic Resonance Spectroscopy and Histology. J Neurotrama 2010; 27:599-610.

[64] Erschbamer M, Oberg J, Westman E, Sitnikov R, Olson L, Spenger C. 1H-MRS in Spinal Cord Injury: Acute and Chronic Metabolite Alterations in Rat Brain and Lumbar Spinal Cord. Eur J Neurosci 2011; 33:678-688.

[65] Solanky BS, Abdel-Aziz K, Yiannakas MC, Berry AM, Ciccarelli O, Wheeler-Kingshott CA. In Vivo Magnetic Resonance Spectroscopy Detection of Combined Gluamate-Glutamine in Healthy Upper Cervical Cord at 3T. NMR Biomed 2013; 26:357-366.

[66] Kachramanoglou C, De Vita E, Thomas DL, Wheeler-Kingshott CA, Balteau E, Carlstedt T, Choi D, Thompson AJ, Ciccarelli O. Metabolic Changes in the Spinal Cord After Brachial Plexus Root Re-Implantation. Neurorrehabil Neural Repair 2013; 27:118-124.